Advancing high impedance fault localization via adaptive transient process calibration and multiscale correlation analysis in active distribution networks

Jian-Hong Gao[a,b,c,d], Mou-Fa Guo[a 1,d], Shuyue Lin[b], and Duan-Yu Chen[c 2]

[a] College of Electrical Engineering and Automation, Fuzhou University, Fuzhou, 350108, China
[b] School of Engineering, University of Hull, Hull, HU6 7RX, UK.
[c] Department of Electrical Engineering, Yuan Ze University, Taoyuan 32003, Taiwan.
[d] Engineering Research Center of Smart Distribution Grid Equipment, Fujian Province University, Fuzhou, 350108, China.

Abstract

Fault localization is crucial for ensuring stability, particularly in high impedance faults (HIF) characterized by low current levels and prolonged transient processes (TP). Existing methods predominantly analyze differences in the fixed-length transient waveform, potentially causing delays in triggering or failure in HIF scenarios. To address these challenges, a novel AI application paradigm for HIF localization was introduced, incorporating both adaptive TP calibration and multiscale correlation analysis. Based on 1D-Unet, the TP of the zero-sequence voltage (ZSV) can be adaptively calibrated to maximize the utilization of transient information. Subsequently, the differential zero-sequence voltage (DZSV) and transient zero-sequence current (TZSC) can be acquired to facilitate multiscale correlation analysis. Combined with a sliding window strategy, the micro correlation between DZSV and TZSC is articulated through the local correlation degree (LCD). The comprehensive correlation degree (CCD) between DZSV and TZSC is then formulated to realize fault feeder/ section localization at the macro level. The 1D-Unet model achieved a classification accuracy of 99.2% for sample points in test datasets and showed robustness with an accuracy exceeding 93.5% in the presence of 20dB noise interference. When integrated with the well-trained 1D-Unet, the proposed approach underwent further validation using simulation data and field recordings. These tests confirmed the model's resilience to noise interference up to 20 dB and its efficacy across networks of diverse topologies, such as the IEEE-13 and 34-node distribution networks. Additionally, an industrial prototype applying this framework identified all fault conditions without false positives or omissions, outperforming existing methods under various fault scenarios, including those involving high impedance materials and different resistance levels across multiple feeders.

Keywords: Active distribution networks, adaptive transient process calibration, fault localization, high impedance fault, multiscale correlation analysis.

Acronyms
HIF: High Impedance Fault
LIF: Low Impedance Fault
SPGF: Single-phase Ground Fault
AI: Artificial Intelligence
TZSV: Transient Zero-sequence Voltage
DZSV: Differential Zero-sequence Voltage
TZSC: Transient Zero-sequence Current
TP: Transient Process
NTP: Non-transient Process
LCD: Local Correlation Degree
CCD: Comprehensive Correlation Degree

1. Introduction

The localization of high impedance fault (HIF) in active distribution networks represents a critical and challenging task, owing to the subtle nature of such faults. As one kind of single-phase ground fault (SPGF), HIF typically occurs in overhead feeders when a live conductor contacts high-resistive materials, such as a tree branch, grass, gravel, or the ground surface [1]. Unlike low impedance faults (LIFs), HIFs generate low-level currents that often evade detection by conventional overcurrent relays, leading to prolonged fault durations. Although the fault current may be less than 10% of the load current and appear innocuous, it poses significant risks due to the arc flash produced by HIF, which can ignite nearby combustible materials, causing fires or personal injury. Thus, prompt and efficient HIF localization is essential to mitigate their effects and prevent subsequent disasters.

With the intricate challenges of HIF localization, artificial intelligence (AI) advancements offer innovative solutions. The impact of AI is notable in various sectors, including industrial control [2], [3], network security [4], [5], and energy management [6], [7]. Incorporating AI into HIF localization enhances performance and adaptability, enabling precise fault localization in complex environments.

Amid rapid AI advancements, significant academic efforts focus on developing AI-based methods for addressing HIF

[1] Corresponding author.
E-mail address: gmf@fzu.edu.cn (M. F. Guo)
[2] Corresponding author.
E-mail address: dychen@saturn.yzu.edu.tw (D. Y. Chen)

issues in active distribution networks. Existing literature broadly categorizes these methods into two groups [8]. The first involves feature extraction and classification, utilizing technologies like wavelet transform [9], S-transform [10], and mathematical morphology [11], followed by classifiers such as random tree [12], fuzzy logic [13], and support vector machine [14] for subsequent classification. The effectiveness of these methods heavily relies on the quality of extracted features, necessitating domain-specific expertise.

The second category adopts an end-to-end approach, reducing reliance on expert knowledge and often yielding superior performance. These methods use original signals or convert them into time-frequency matrices as input for deep learning models, such as convolutional neural networks [15], variational prototyping-encoder [16], and fully convolutional network [17], aiming to categorize samples into predefined groups for macro classification. However, most AI-based methods lack specific designs for the unique requirements of HIF localization.

Inspired by [18], the embedded semantic features in electrical signals strongly suggest the potential functionality of waveform morphology, especially in the transient stage of HIF, for sample point classification tasks. Accordingly, the Unet model, applied to HIF diagnosis [19], demonstrates a robust capability to extract local and global features. It primarily utilized the first detected sample point as the fault moment yet overlooked the transient information's utility. Despite its original design for 2D image segmentation, where each pixel requires labeling for a final result, the Unet structure parallels the image segmentation task. Classifying each signal sample point is essential for this paper's adaptive TP calibration for HIF localization. Unet's adaptation to 1D sequential data, as demonstrated in [19], makes it a suitable tool for this task.

Therefore, this paper introduces a novel HIF localization method using adaptive TP calibration and multiscale correlation analysis. This method capitalizes on the Unet architecture's feature extraction capabilities. Initially, the 1-D Unet model captures the complete transient information during HIF. Subsequently, a sliding window strategy is applied to the differential zero-sequence voltage (DZSV) and transient zero-sequence current (TZSC). This strategy computes the local correlation degree (LCD) on a microscale and establishes a comprehensive correlation degree (CCD) on a macroscale for fault feeder/section localization. The primary contributions of this paper have been articulated to include:

1. The introduction of an adaptive TP calibration utilizing semantic segmentation technology, specifically the 1D-Unet model, for precise fault feeder/section localization has been detailed. This method has been shown to significantly reduce the misjudgments of fault moments, thereby refining the accuracy of fault-triggering analysis.
2. The integration of a sliding window strategy with multiscale correlation analysis for segmenting TZSC and DZSV has been described. This approach has been demonstrated to efficiently calculate the LCD on a micro-scale and establish a practical HIF localization criterion by quantifying the CCD between TZSC and DZSV on a macro-scale. The approach's effectiveness has been validated through extensive simulations under various conditions, including noise interference and topology variations.
3. The development of an industrial prototype incorporating the proposed approach has been presented. This prototype, featuring an innovative hardware structure and software framework for real-time multitasking, is effective through comparative analysis using a 10kV full-scale test system, highlighting its superiority over current typical methods.

The rest of the paper is organized as follows: Section 2 reviews recent works on HIF fault localization. Section 3 presents the transient analysis of HIF. Section 4 details the proposed fault localization approach. Simulation verification is described in Section 5, adaptability analysis is in Section 6, and experimental verification is in Section 7. Finally, Sections 8 and 9 summarize the main work and discuss its limitations and future research directions.

2. Related work

The heightened interest in HIF continues to shape research directions, with recent studies broadly classifying the methods for HIF localization into three categories: original signal-based, signal processing-based, and AI-based.

The original signal-based approach derives spatial and temporal distribution rules from theoretical HIF analysis, enabling the identification of the fault feeder or sections and the precise HIF location. Study [20], for instance, utilizes slope relationships to identify faulted feeders, while [21] employs cross-correlation coefficients, considering waveform disparities and transient zero-sequence energy. Research [22] concentrates on transient energy and cosine similarity, and [23] applies dynamic voltage-current profiling of zero-sequence quantities. Furthermore, [24] uses time-frequency characteristics of traveling waves and quadratic B-spline wavelet analysis for fault distance estimation. However, based on these methods, the theoretical analysis of HIF often assumes ideal conditions. In reality, distribution networks are more complex, with variable loads, diverse configurations, and unpredictable external factors.

Signal processing-based methods involve a variety of advanced technologies for handling electrical signals to establish effective fault localization criteria. In [25], the TZSC is divided into steady-state and transient components, with the fast Fourier transform employed to isolate the transient component. Subsequently, steady-based and transient-based criteria are formulated to identify the fault feeder. Study [26] decomposes TZSC into multiple frequency scale models using a variant of empirical mode decomposition, wherein mode energy and waveform polarity of TZSC are computed for fault feeder detection. Similarly, [27] employs variational mode decomposition to isolate intrinsic mode functions (IMFs), focusing on those with the highest kurtosis. These IMFs are then analyzed using Teager–Kaiser energy operators (TKEOs) and segmented into subintervals for calculating time entropy values for HIF localization. In [28], the method includes using empirical wavelet transform to break down differential faulty energy into time-frequency components, selecting the highest permutation entropy component, and then applying a permutation variance index for HIF detection. Despite their effectiveness, these signal processing methods require precise threshold adjustments and extensive trial-and-error for hyperparameter selection, like the mother wavelet in wavelet transform, limiting their practical adaptability in dynamic network environments.

AI-based methods, particularly deep learning, are increasingly recognized for their effectiveness in HIF fault localization, offering a notable edge over traditional machine learning algorithms. These deep learning models capitalize on their capacity to independently learn from extensive data sets and apply diverse architectural frameworks. In [29], first-half waveforms are inputted into a well-trained convolutional neural network, where the accuracy of localization hinges on the precise determination of the fault moment. [30] advances a two-path fully convolutional network by integrating semantic segmentation, thereby enhancing the precision of fault identification and localization in waveform signals. These deep learning-based HIF localization methods predominantly utilize direct outputs from deep learning models, producing qualitative results. This protection paradigm, lacking in decision-making interpretability, fails to gain acceptance and trust among power system protection experts, who prioritize clear, explainable processes for safety and reliability.

The primary research objective for fault localization among the discussed methods is analyzing the fault's TP. Regarding HIF characteristics, the duration of TP varies based on specific fault scenarios. However, methods above that rely on fixed-length measured signals struggle to adapt to this variation, and estimation errors in the fault moment can impact the final fault localization results. To address these issues, this paper introduces a split-and-conquer strategy for a step-by-step implementation of HIF localization. Initially, the 1D-Unet semantic segmentation model was utilized to adaptively calibrate the TP of HIF, treating the unique transient waveform as a semantic feature. This approach is complemented by a multiscale correlation analysis throughout the transient information of HIF, calculating the LCD on a micro-temporal scale and establishing a CCD for a macro-temporal scale to realize fault feeder/section localization.

3. Transient analysis of high impedance fault

As illustrated in Fig. 1, an HIF occurs within an active distribution network that includes a neutral point grounded through a Peterson coil, characterized by fault resistance R and the coil's inductance represented as L.

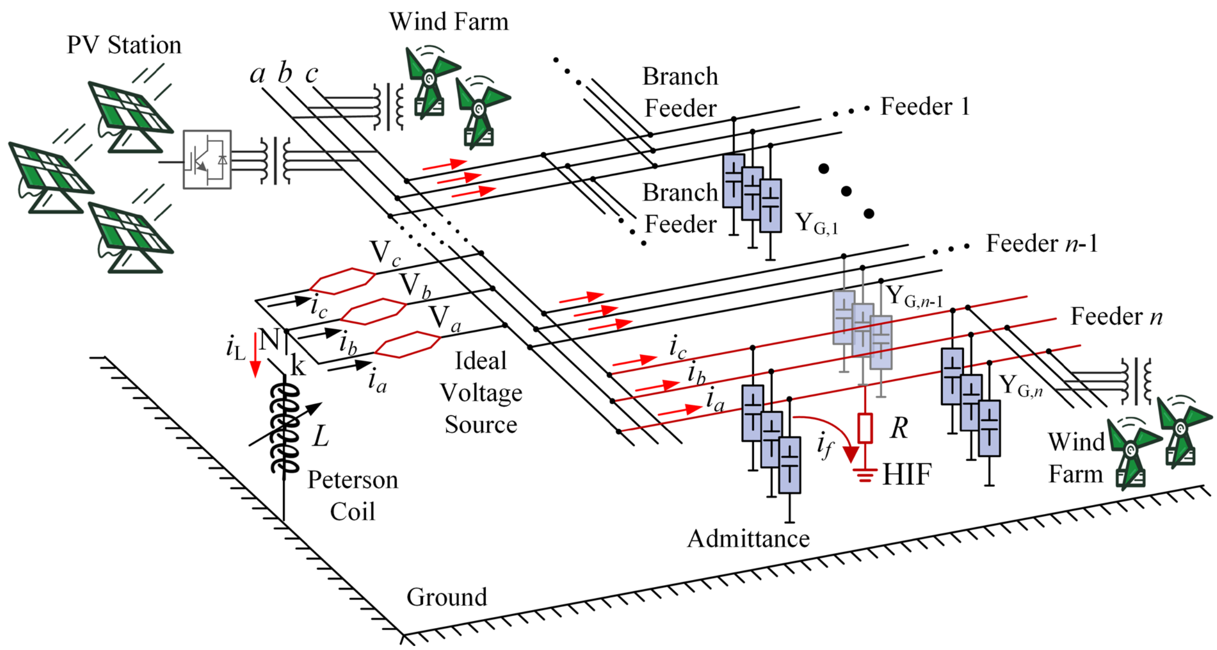

Fig. 1. HIF occurs in the active distribution network.

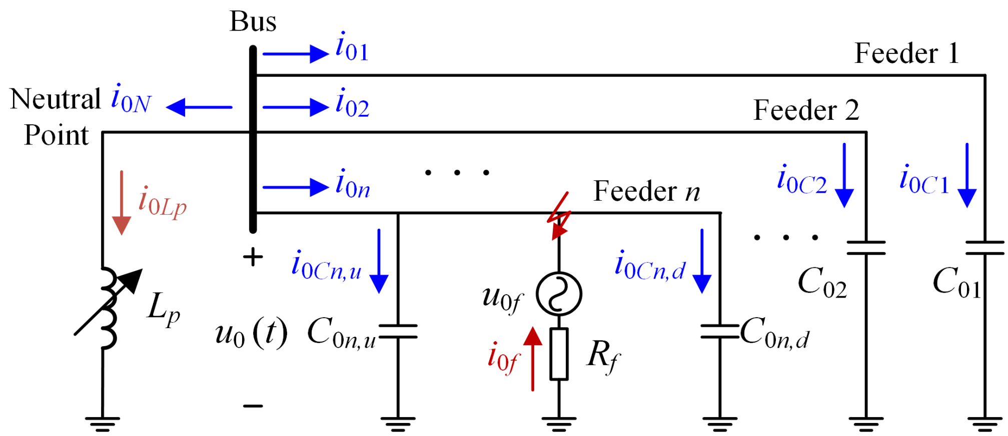

Fig. 2. Equivalent circuit of HIF.

According to [31], when distribution generation (DG) is connected to the active distribution networks, it adopts an Δ/Y transformer. Therefore, the zero-sequence equivalent network with DG is completely consistent with that without DG, as shown in Fig. 2, wherein the equivalent fault resistance R_f and inductance L_p are threefold the values of R and L from Fig. 1, respectively. Moreover, C_{0k} (where k=1,2,..,n-1) denotes the zero-sequence capacitance of sound feeder k, while $C_{0n,u}$ and $C_{0n,d}$ represent the upstream and downstream zero-sequence capacitances at the fault point.

According to Fig. 2, the established equation is as follows:

$$\begin{aligned} i_{0f} &= i_{0N} + \sum_{i=k}^{n} i_{0k} = i_{0L_p} + i_{0C\Sigma} \\ &= i_{0L_p} + \sum_{i=k}^{n-1} i_{0Ck} + i_{0Cn,u} + i_{0Cn,d} \end{aligned} \tag{1}$$

Where i_{0Lp} is the ZSC of the Peterson coil, i_{0k} is the ZSC of sound feeder k, $i_{0C\Sigma}$ is the aggregate zero-sequence capacitance current, i_{0Ck} denotes the zero-sequence capacitance of the sound feeder k. $i_{0Cn,u}$ and $i_{0Cn,d}$ are the fault point's upstream and downstream zero-sequence capacitance.

Additional equations (2) and (3) elucidate the ZSC distribution among the fault feeder and sound feeders:

$$i_{0k} = i_{C0k} = C_{0k}\frac{\mathrm{d}u_0}{\mathrm{d}t} \tag{2}$$

$$i_{0n} = -(i_{0C\Sigma} - i_{0Cn,u} - i_{0L_p}) = i_{0L_p} - (C_{0\Sigma} - C_{0Cn,u})\frac{\mathrm{d}u_0}{\mathrm{d}t} \tag{3}$$

Where $C_{0\Sigma}$ is the total zero-sequence capacitance of the network, and du_0/dt is the derivative of the ZSV.

Analysis of (2) and (3) shows a positive correlation between ZSC and DZSV in sound feeders but a partial negative correlation in fault feeders, especially during post-fault transients. The key difference is in their ZSC composition: fault feeders contain fault current and zero-sequence capacitance currents, while sound feeders only have the latter. By deploying multiple measurement devices along a feeder, differentiation between fault feeder characteristics upstream and sound feeder attributes downstream of the fault point is achievable. Therefore, leveraging the ZSC-DZSV relationship is crucial for fault feeder/section localization, which includes detecting fault feeders or sections.

Observations from fault data show that the dynamic changes from fault inception to arc generation align with a constant coefficient second-order differential equation, which indicates the suitability of a linear model for analyzing the transient stage of HIF. In this context, R_f can be considered constant, and a second-order constant coefficient differential equation, depicted in (4), can represent Fig. 2.

$$R_f C_{0\Sigma} L_\mathrm{p} \frac{\mathrm{d}^2 i_{0L_\mathrm{p}}}{\mathrm{d}t^2} + L_\mathrm{p}\frac{\mathrm{d}i_{0L_\mathrm{p}}}{\mathrm{d}t} + R_f i_{0L_\mathrm{p}} = u_0(t) \tag{4}$$

In this context, the decay coefficient δ of the second-order equation can be defined as in (5).

$$\delta = \frac{1}{2R_f C_{0\Sigma}} \tag{5}$$

The decay coefficient reflects the transient stage's duration, which is important for fault detection. While previous research acknowledges HIF's extended transient phase, its exact duration remains elusive due to randomness. The gradual nature of HIF also causes delayed fault detection in practical, threshold-based methods. Therefore, the proposed approach introduces adaptive TP calibration to effectively utilize the transient phase to enhance the fault feeder/section localization performance.

4. Fault localization approach

4.1 Adaptive Transient Process Calibration

Semantic segmentation, vital in computer vision, labels each pixel for pixel-level object identification, enhancing recognition and localization. Particularly impactful in medical fields, including ECG analysis, it segments images into regions for detailed analysis [18], [32]. In ECG analysis, classifying signal sample points improves HIF diagnosis, a novel AI application in power systems. This method, distinct from traditional classification and regression, employs the modified 1D-UNet for HIF triggering, initially focuses on the transient stage's start point post-fault [18], but does not fully utilize the complete TP. The updated approach uses the 1D-Unet for adaptive TP calibration, optimizing AI for fault feeder/section localization.

The 1D-Unet, illustrated in Fig. 3, adapts the original Unet for 1D inputs like time-series data. Its encoder, with three layers, downsamples data via convolution and max-pooling, later restoring size and merging detail levels. The architecture's final layer categorizes points into TP or non-TP (NTP), assessed against actual values using the cross-entropy loss function.

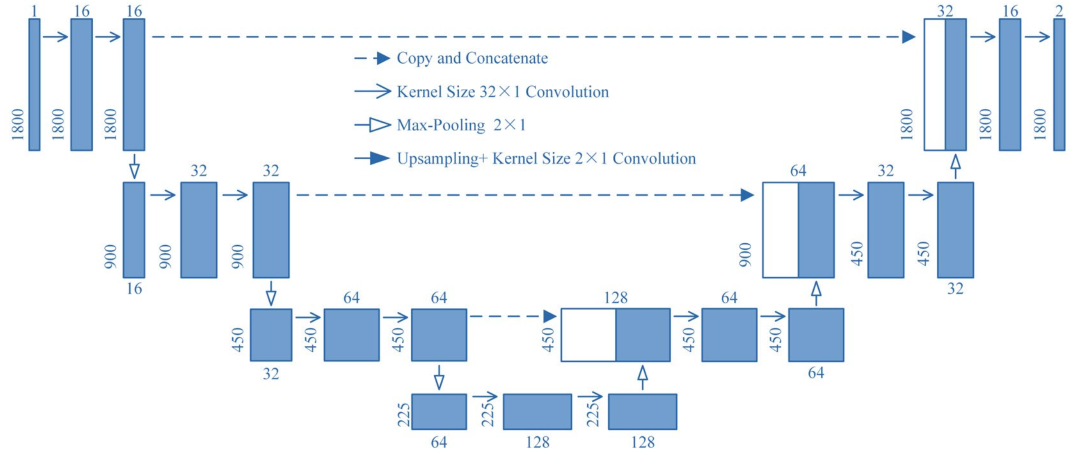

Fig. 3. Architecture of 1D-Unet.

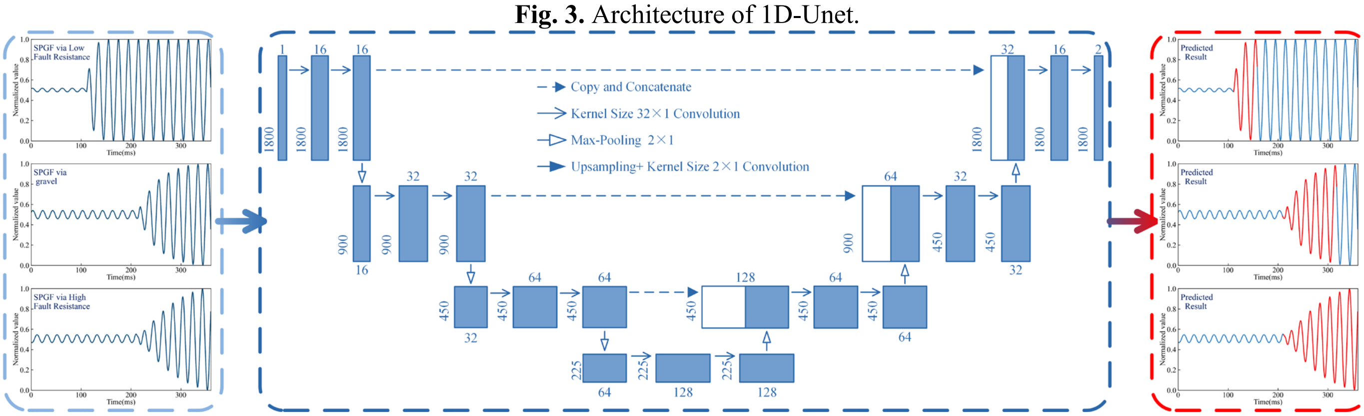

Fig. 4. Adaptive transient process calibration by trained 1D-Unet.

Existing literature presents various methods for the TP of SPGF using fixed-length data, spanning from half to several frequency cycles. However, the duration of TP varies with on-site conditions. Our study utilizes a 1D-Unet model for adaptive TP calibration, enhancing fault feeder/section localization (refer to Fig. 4). This trained model processes the ZSV to produce TZSV, previously applied in fault triggering [19].

Fig. 5 and Fig. 6 depict two SPGF scenarios with different fault resistances, contrasting HIF and LIF. In Fig. 5, the TZSV duration is much shorter with a low fault resistance (200 Ω) than a high one (3000 Ω). Fig. 5(b) and Fig. 6(b) show a reversal in TZSC direction between fault and sound feeders, aligning with (2) and (3). Integrating these waveforms into combined diagrams (Fig. 5(c), 5(d), 6(c), 6(d)) allows a detailed examination of the DZSV and TZSC relationship.

Analysis of DZSV reveals that in sound feeders, TZSC polarity matches DZSV, while in fault feeders, there's a slight waveform deviation. DZSV and ZSC display minimal changes in fault or sound feeders during steady-state. Therefore, richer in diagnostic information, the transient information warrants greater focus on a macro temporal scale for SPGF diagnosis.

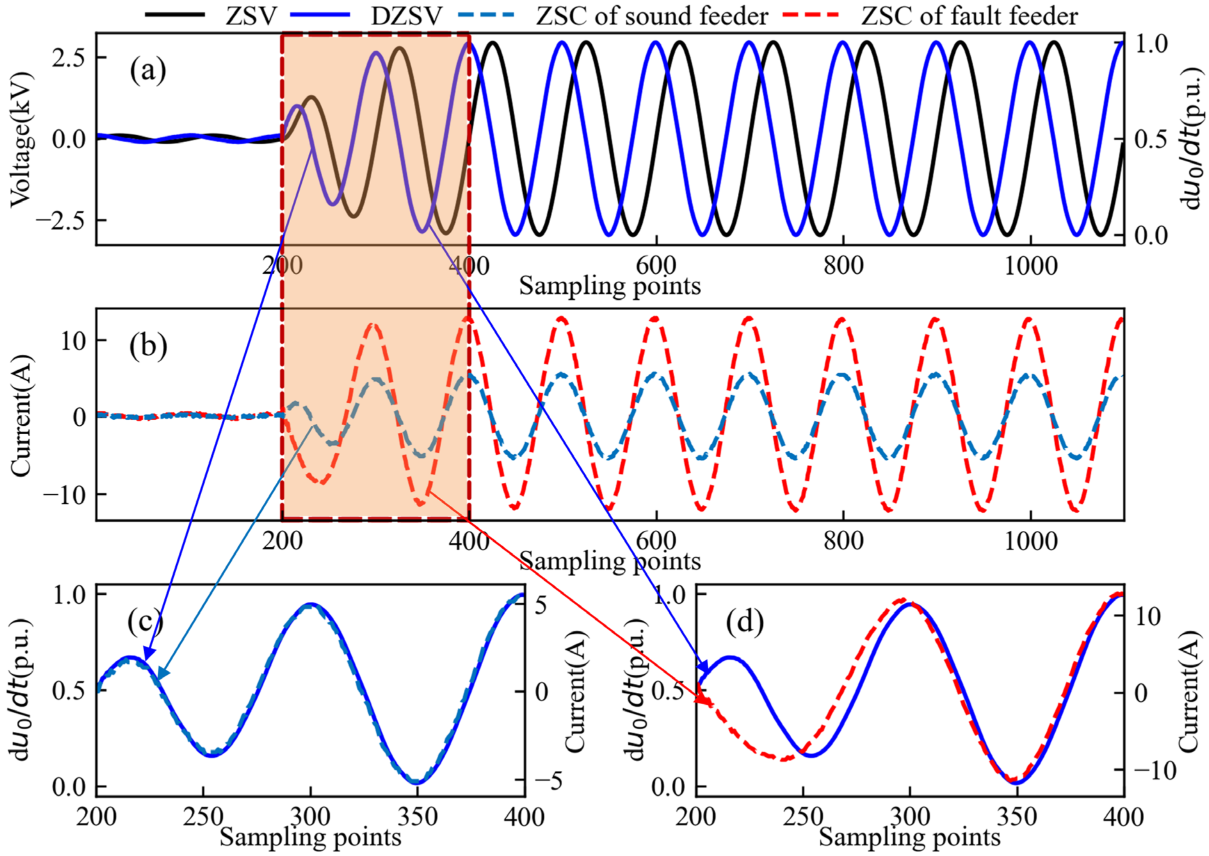

Fig. 5. SPGF within low fault resistance. (a) ZSV and its DZSV. (b) ZSCs of fault and sound feeders. (c) DZSV and TZSC of the sound feeder. (d) DZSV and TZSC of fault feeder.

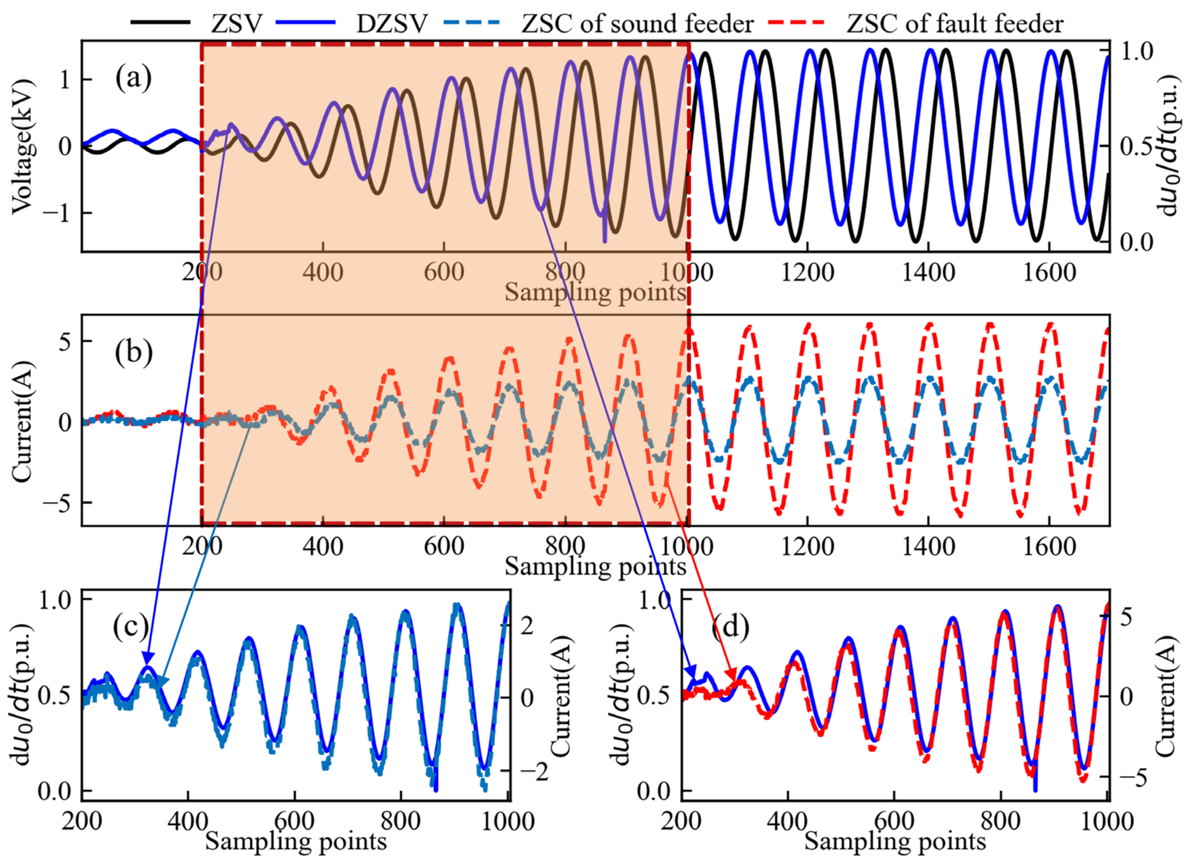

Fig. 6. SPGF within high fault resistance. (a) ZSV and its DZSV. (b) ZSCs of fault and sound feeders. (c) DZSV and TZSC of the sound feeder. (d) DZSV and TZSC of fault feeder.

4.2 Multiscale Correlation Analysis

After calibrating the TP of DZSV using the 1D-Unet model, a sliding window strategy was introduced for analyzing the micro-temporal correlation between DZSV and ZSC. This strategy involves setting the sliding window's length and stride to half a frequency cycle and one sampling interval operating at a 5 kHz sampling rate. Subsequently, the Pearson correlation coefficient was adopted and shown (6) to quantify the LCD difference between DZSV and TZSC.

$$\mathrm{LCD}=\frac{\sum_{i=1}^{n}\left(x_i-\overline{x}\right)\left(y_i-\overline{y}\right)}{\sqrt{\sum_{i=1}^{n}\left(x_i-\overline{x}\right)^2}\sqrt{\sum_{i=1}^{n}\left(y_i-\overline{y}\right)^2}} \tag{6}$$

Where x_i and y_i denote the individual observations of the two input variables while $\overline{x}$ and $\overline{y}$ represent their respective mean value.

After implementing adaptive TP calibration, the LCD curve is computed as shown in Fig. 7. In the fault feeder, the initial LCD values are below zero, gradually increasing towards 1. In contrast, the sound feeder's LCD curve stays positive, initially lower due to high-frequency components. Fig. 7(c) and (e) reveal extreme minimum points in the LCD curve, coinciding with DZSV's extreme points. Incorporating (2) allows for constructing the CCD, as outlined in **Algorithm 1**. This method effectively localizes faults, indicating fault feeders/sections with negative CCD values and sound feeders/sections with positive ones.

Algorithm 1: Calculate CCD

Input: DZSV, LCD, stride
Output: CCD

```
ExtIdx=[], NegIdx=[], MinLCDIdx=[], CCD=0
for i from 1 to (length(DZSV)-2) do
    if DZSV[i] > DZSV[i-1] and DZSV[i] > DZSV[i+1] then
        ExtIdx.append(i)
    else if DZSV[i] < DZSV[i-1] and DZSV[i] < DZSV[i+1] then
        ExtIdx.append(i)
    end if
end for
for i from 0 to (length(LCD) - 1) do
    if LCD[i] < 0 then
    NegIdx.append(i)
    end if
end for
for i in ExtIdx do
    startIdx=i * stride
    endIdx=min((i + 1) * stride, len(LCD))
    minLCDIdx=startIdx + argmin(LCD[startIdx:endIdx])
    MinLCDIdx.append(minLCDIdx)
end for
unionIdx=sorted(set(NegIdx) | set(MinLCDIdx))
for i from 0 to (len(unionIdx) - 1) do
    CCD=CCD + LCD[unionIdx[i]]
end for
return
```

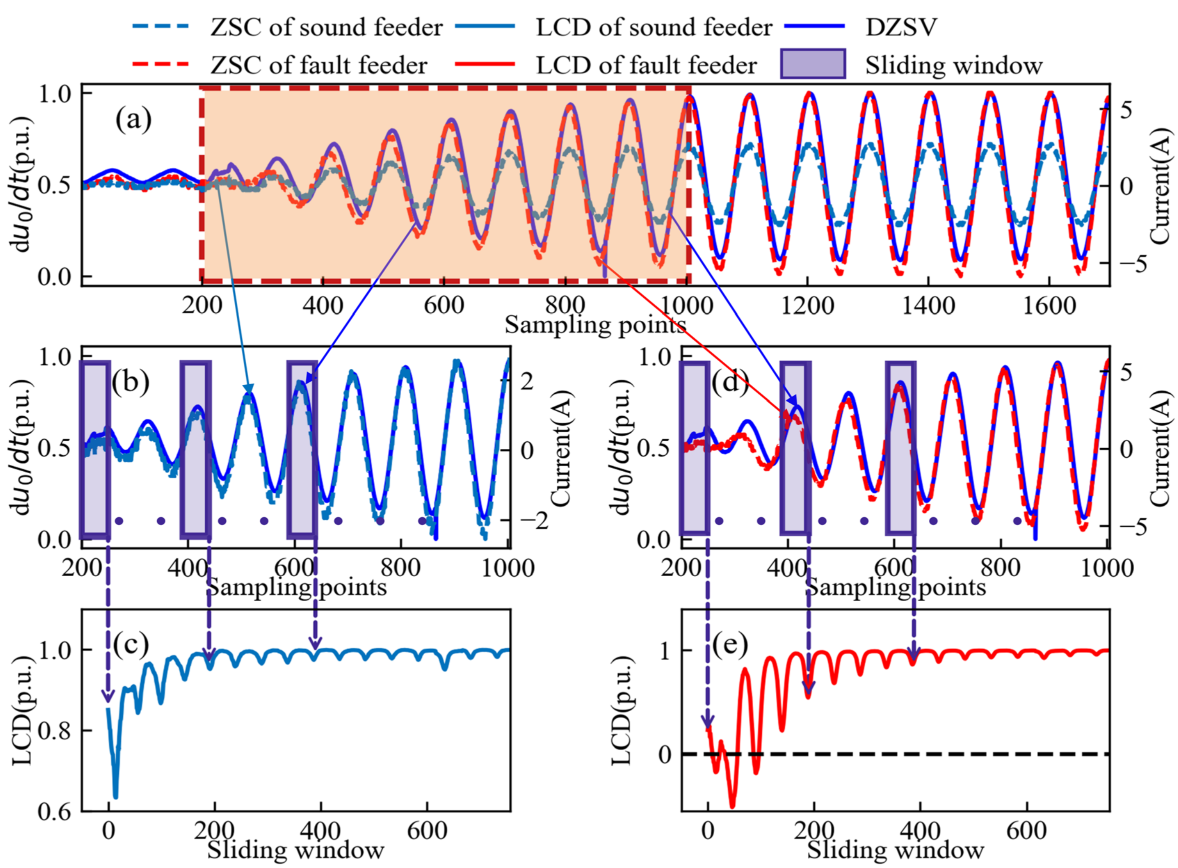

Fig. 7. Calculation of the LCD curve. (a) DZSV and ZSCs of fault and sound feeders. (b) DZSV and TZSC of the sound feeder. (c) LCD curve of sound feeder. (d) DZSV and TZSC of fault feeder. (e) LCD curve of fault feeder.

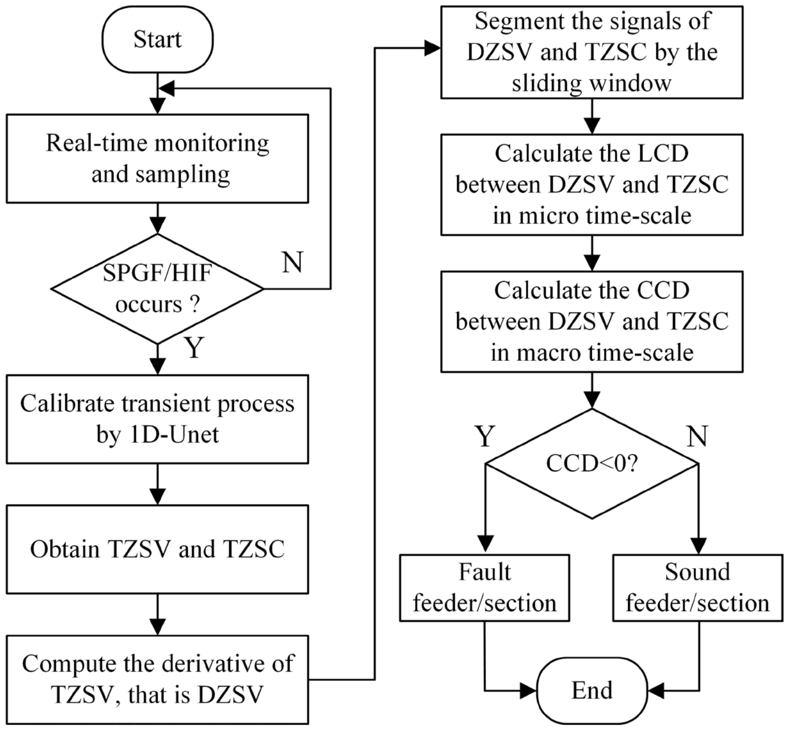

Fig. 8. Flowchart of the proposed approach.

4.3 Workflow of the proposed approach

The proposed approach has employed a 1D-Unet model to meticulously calibrate the TZSV, capturing the entire transient stage following an SPGF event. The derivation of DZSV from TZSV and the segmentation of both TZSC and DZSV waveforms using a sliding window have established a foundation for precise fault analysis. The LCD has been computed at a micro time scale. The CCD between TZSC and DZSV has been assessed at a macro scale, establishing a comprehensive criterion for localizing faults in feeders and sections. This structured approach is visually represented in Fig. 8.

The steps in the flowchart include:

Step 1: **Real-time monitoring:** The proposed approach begins with real-time monitoring to detect SPGFs or HIFs promptly, using our team's fault-triggering algorithms [19].

Step 2: **Adaptive transient process calibration:** Upon detection of SPGF or HIF, the TP has been calibrated using the 1D Unet model, yielding the TZSV and TZSC.

Step 3: **Derivation of DZSV:** The DZSV has been derived from the TZSV, crucial for subsequent fault characteristic analysis.

Step 4: **Data segmentation by sliding window**: The TZSC and DZSV waveforms have been segmented using a sliding window, setting the stage for detailed correlation analysis.

Step 5: **LCD calculation**: The LCD has been computed at the micro time scale, providing a granular view of the signal correlations as per (6).

Step 6: **CCD evaluation**: At the macro time scale, the CCD has been evaluated, offering a comprehensive overview of the signal correlations over time, as described in **Algorithm 1.**

Step 7: **Fault Localization Decision:** The decision on fault localization has been based on the CCD value, where a negative value indicates a fault in a feeder or section, and a positive value signifies a sound feeder or section.

5. Simulation Verification

5.1 Simulation Setup

In this study, a 1D-Unet model is trained using fault data from PSCAD/EMTDC simulations to address the challenge of obtaining sufficient practical data. A 10 kV distribution network with five feeders is modeled in Fig. 9, with each feeder based on real line parameters using a mid-frequency variable parameter model in PSCAD/EMTDC. Table 1 details the different feeder types and parameters, where R_1, L_1, and C_1 represent positive-sequence parameters, and R_0, L_0, and C_0 represent zero-sequence parameters. The SPGF data from PSCAD simulations tend to be more idealized than real field fault data, mainly due to a slight system imbalance in the normal state, where the zero-sequence voltage amplitude is not exactly zero before a fault. To better replicate real-world conditions, the system imbalance was set to 2% in the simulations [33].

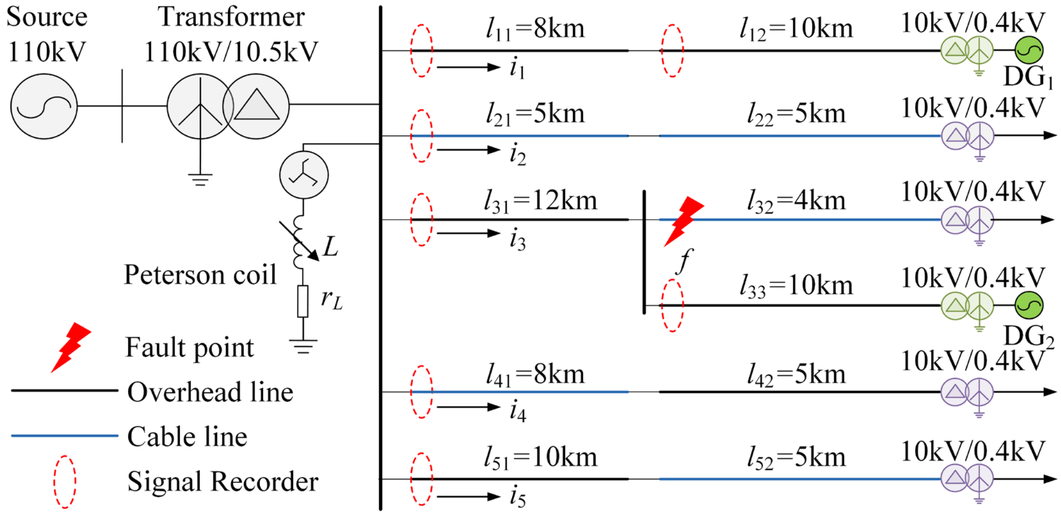

Fig. 9. PSCAD model of the 10 kV active distribution network.

5.2 Dataset Construction

The proposed 1D-Unet model, a type of semantic segmentation, requires detailed data annotation at the sample point level. To overcome the absence of existing tools for annotating electrical signals, the proprietary software LabelSig, accessible on GitHub [34], was utilized for sample-point-level annotation, facilitating the construction of the dataset. A Python script was developed to initialize the PSCAD model, selecting fault points, fault resistances (FRs), and fault initial angles (FIAs) as in Table 2 for fault characterization. This setup automatically runs the PSCAD model, representing the distribution system, and generates simulation data in COMTRADE 99 format. Data annotation is conducted with LabelSig, which processes COMTRADE files to manually annotate the TP fraction in the ZSV waveform. These annotated data would be archived with the COMTRADE files, forming the dataset's foundation for training and testing the model.

The assembled dataset comprises 1000 simulation records. Each record consists of 18 frequency-cycle waveforms at a sampling frequency of 5k Hz, resulting in 1800 sample points per record. Following data annotation, each sample point is assigned a corresponding label, culminating in 1.8 million pairs of sample points and their respective labels.

Table 1
Feeder parameters of 10 Kv active distribution network

Type	*R* (Ω/km)		*L* (mH/km)		*C* (μF/km)	
	R_1	R_0	L_1	L_0	C_1	C_0
Overhead line	0.17	0.23	1.21	5.48	0.0097	0.006
Cable line	0.098	0.246	0.274	0.955	0.351	0.166

Table 2
The configuration of diverse fault conditions

Fault feeder	FIA(°)	FR(Ω)	Quantity
l_1,l_2,l_3,l_4,l_5	0~ 90 per 15	200, 300, 500, 1000, 1500, 2000, 3000	1000

5.3 Model Implementation

Table 3 shows that all simulation records were divided into training and testing subsets at a 70:30 ratio. The number of TP sample points for each record varies with the fault's duration, resulting in a fluctuating proportion of sample point categories in the training and testing datasets. The training and testing were performed on a system equipped with a 3.2 GHz Intel® Core™ i7-8700 processor, 16GB RAM, and an NVIDIA® GeForce RTX-1060 graphics card, using the TensorFlow platform. Hyperparameter optimization, essential for achieving optimal model performance, was systematically conducted through a trial-and-error process, as indicated in Table 4. This process determined an initial learning rate of 0.001, a training length of 100 epochs, and a batch size 32. The model utilized the Adam optimizer and a CrossEntropy loss function for parameter updates. Strategies such as dropout, early stopping, and learning rate decay were crucial in preventing overfitting and ensuring efficient learning.

Table 3
Distribution of the dataset for training and testing

Dataset	Simulation records	Sample points	
	Quantity	Category	Quantity
Training	700	TP	189298
		NTP	1070702
Testing	300	TP	87116
		NTP	452884

Table 4
Hyperparameter of the 1D-Unet

Hyperparameter	1D-Unet
Learning rate	0.001
Training epoch	100
Batch size	32
Optimizer	Adam
Loss function	CrossEntropy
Training Strategy	Dropout, Early stop, Learning rate decay

The model leveraged the Adam optimizer with a cross-entropy loss function in parameter optimization. The Adam optimizer was selected for its adaptive learning rate mechanism, which facilitates efficient parameter updates. The cross-entropy loss function, depicted in (7), was the chosen objective function. It excels in classification scenarios by measuring the disparity between predicted probabilities and actual class labels. The primary objective was to minimize this cross-entropy, thus aligning the predicted probabilities more closely with the actual labels. By optimizing this loss function, the Adam optimizer's dynamic adjustment of learning rates enabled the model to iteratively refine its weights iteratively, enhancing the precision of its predictions throughout the training phase.

$$H(y,\hat{y}) = -\sum_{i=1}^{N}\sum_{j=1}^{C} y_{ij}\log(\hat{y}_{ij}) \tag{7}$$

Where y_{ij} denotes the presence or absence of class j in the actual labels for sample i, $\hat{y}_{ij}$ is the predicted probability of class j for sample i, N is the total number of samples, and C is the number of classes.

Furthermore, techniques like dropout and early stopping were employed to combat overfitting. Dropout randomly turns off a fraction of neurons during training, enhancing model robustness, while early stopping terminates training when no significant improvement is observed on a validation dataset. A learning rate decay strategy further ensured faster initial convergence and subsequent training stability. Additionally, for operationalizing the trained 1D-Unet model, a Raspberry Pi served as the central module in an industrial prototype. The RaspPi offers a cost-effective and practical solution for embedded AI computing devices, meeting the computational and speed requirements necessary for our approach. Detailed information about the industrial prototype is provided in Section 6.1.

5.4 Performance Evaluation

The efficacy of the 1D-Unet model in adapting TP calibration for SPGF has been confirmed through tests cited in reference [19]. These tests effectively differentiate sample points associated with the TP of a fault. The 1D-Unet model accurately discerns SPGF or HIF transient waveforms by clustering adjacent samples within the same category. The model's performance was assessed based on the accuracy of sample point classification, as described by the equation in (8).

$$\text{Accuracy} = \frac{\text{Number of correctly classified sample points}}{\text{Total number of sample points}} \tag{8}$$

In Fig. 10, the classification capabilities of the 1D-Unet model are illustrated. Fig. 10(a) presents an accuracy curve, demonstrating a plateau in testing accuracy and initiating an early stop at epoch 71. Fig. 10(b) shows a loss curve that indicates a consistent decrease over epochs, signifying learning stability. The confusion matrix in Fig. 10(c) reveals high classification accuracies of 99.1% for TP sample points and 99.7% for NTP sample points. These findings collectively confirm the model's high precision, with an overall testing accuracy of 99.2%, thereby validating its effectiveness in differentiating between TP and NTP sample points in detecting SPGF, even under HIF conditions.

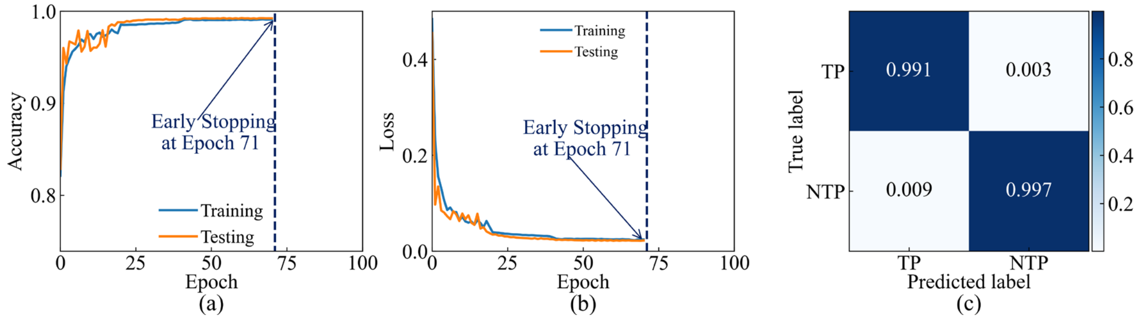

Fig.10. Visualization of the 1D-Unet training process. (a) Training and testing accuracy curves. (b) Training and testing loss curves. (c) Confusion matrix for sample point classification.

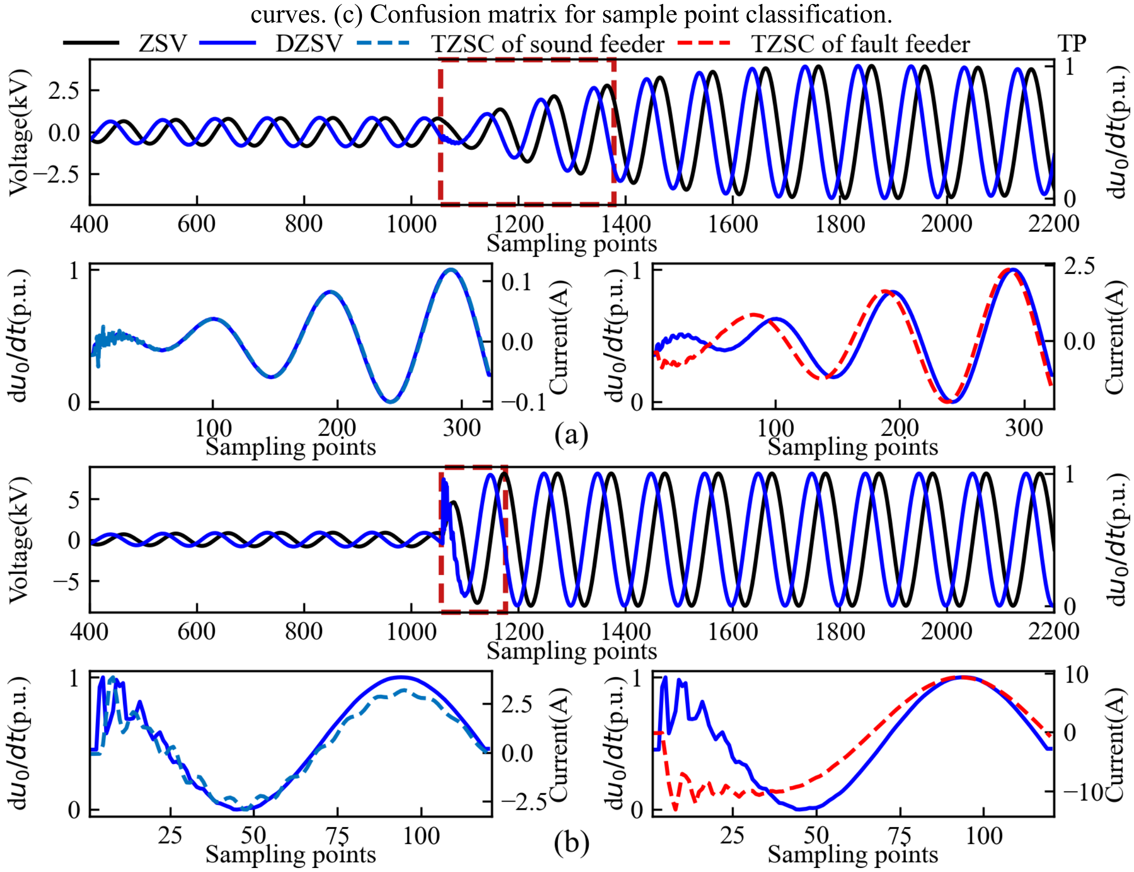

Fig. 11. Case study (a) HIF of l_2 fault under 3000Ω, (b) LIF of l_2 fault under 200Ω.

Upon determining the TP of ZSV, multiscale correlation analysis was performed to detect fault feeders or locate fault sections based on specific needs like feeder identification or section location. To illustrate the proposed method, two scenarios were presented in Fig. 11, showcasing HIF and LIF occurrences at feeder l_2, characterized by fault resistances of 200 Ω and 3000 Ω, respectively.

Fig. 11 indicates the diverse transient waveform's length between HIF and LIF, with the former being larger than the latter. Moreover, the disparity between DZSV and TZSC could be harnessed to detect the faulty feeder. The transient information under both SPGFs was enclosed in a red dashed box, subsequently utilized by the multiscale correlation analysis to compute the CCD for each feeder. The associated results are presented in Table 5. It can be deduced from the table that regardless of the occurrence of HIF or LIF, the CCD of fault feeder l_2 is negative and opposed to those of other sound feeders.

Table 5

CCD Under different fault conditions

Type of SPGF	Sound feeder	Fault feeder
HIF	0.686	**-0.547**
LIF	0.893	**-0.504**

5.5 Adaptability analysis

This paper expands upon the previous work published in [19], detailing an adaptability analysis of the proposed 1D-Unet model. This section focuses primarily on the adaptability analysis associated with multiscale correlation within the context of the proposed fault feeder/section localization approach.

5.5.1 Noise Interference

Recognizing the impact of environmental noise on the effectiveness of our proposed approach, we deliberately introduced noise into the ZSV and ZSC signals. This procedure aimed to evaluate the performance of TP calibration and multiscale correlation analysis. Notably, environmental noise influences the ZSV and ZSC signals in disparate ways, driving the signal-to-noise ratio (SNR) variability of these signals. Under normal circumstances, the ZSV signal experiences no noise interference. We elected an extreme condition, characterized by an SNR of 20dB,as shown in Fig.12, to appraise the sample point classification performance of our proposed 1D-Unet. A series of test results, depicted in Table 6, suggest that the accuracy of the 1D-Unet is susceptible to noise interference, with escalating noise levels causing a decrement in accuracy. Table 6 also shows that the 1D-Unet model can achieve an accuracy exceeding 93.5%, even in the presence of 20dB noise interference.

Contrarily, to assess the efficacy of multiscale correlation analysis, we introduced noise solely into the ZSC signal, treating the ZSV signal as the ideal case. This operation aligns with most field fault records, suggesting that the ZSC signal typically harbors more noise than the ZSV signal.

Table 6

Performance of 1D-Unet under noise interference

SNR(dB)	20	25	30	35
Accuracy(%)	93.5	95.2	96.8	97.2

After implementing the TP calibration using the 1D-Unet model, an SPGF was introduced as a test case to inject noise, successfully achieving an SNR of 20 dB within the TZSC. In this scenario, feeder l_2 is subjected to a fault characterized by an FIA of 30° and an FR of 3000 Ω, as illustrated in Fig. 12. Fig.12 (a) showcases the TZSV and its derivative, DZSV. Fig. 12(b) through Fig. 12(f) reveal the significant influence of intense noise on the TZSC, which obscures the clear identification of the fundamental fault characteristics of the fault feeder l_2 from the sound feeders l_1, l_3, l_4, and l_5 within the noisy TZSC context. It is particularly noted that during the SPGF event, the polarity relationship between the DZSV and TZSC of the faulted feeder l_2 is inverted, in stark contrast to the consistent polarity observed in the DZSV and TZSC of the non-faulted feeders l_1, l_3, l_4, and l_5. This key observation underscores that, despite intense noise, the polarity relationship between TZSC and DZSV does not change fundamentally, whether in the fault feeder or the sound feeders.

Table 7 provides detailed CCD values for each feeder under varying levels of noise interference, starting with an SNR of 20 dB. At this level, the CCD for the fault feeder l_2 is distinctly negative (-0.314), sharply differentiating it from the positive values observed for the sound feeders l_1 (0.148), l_3 (0.204), l_4 (0.134), and l_5 (0.184). This negative value unequivocally identifies feeder l_2 as the fault feeder. This pattern persists across different SNR levels, with the fault feeder l_2 consistently exhibiting negative CCD values, even as the SNR is increased to 25 dB (-0.339), 30 dB (-0.345), and 35 dB (-0.345).

Fig. 13, which visualizes the data from Table 7, further elucidates this phenomenon by depicting the consistently negative CCD values of feeder l_2 under four distinct conditions of noise interference, thereby affirming its status as the fault feeder with remarkable precision. The unwavering detection of feeder l_2 as the fault feeder, evidenced by negative CCD values across all evaluated SNR levels, attests to the fault localization strategy's efficacy and superior noise resistance.

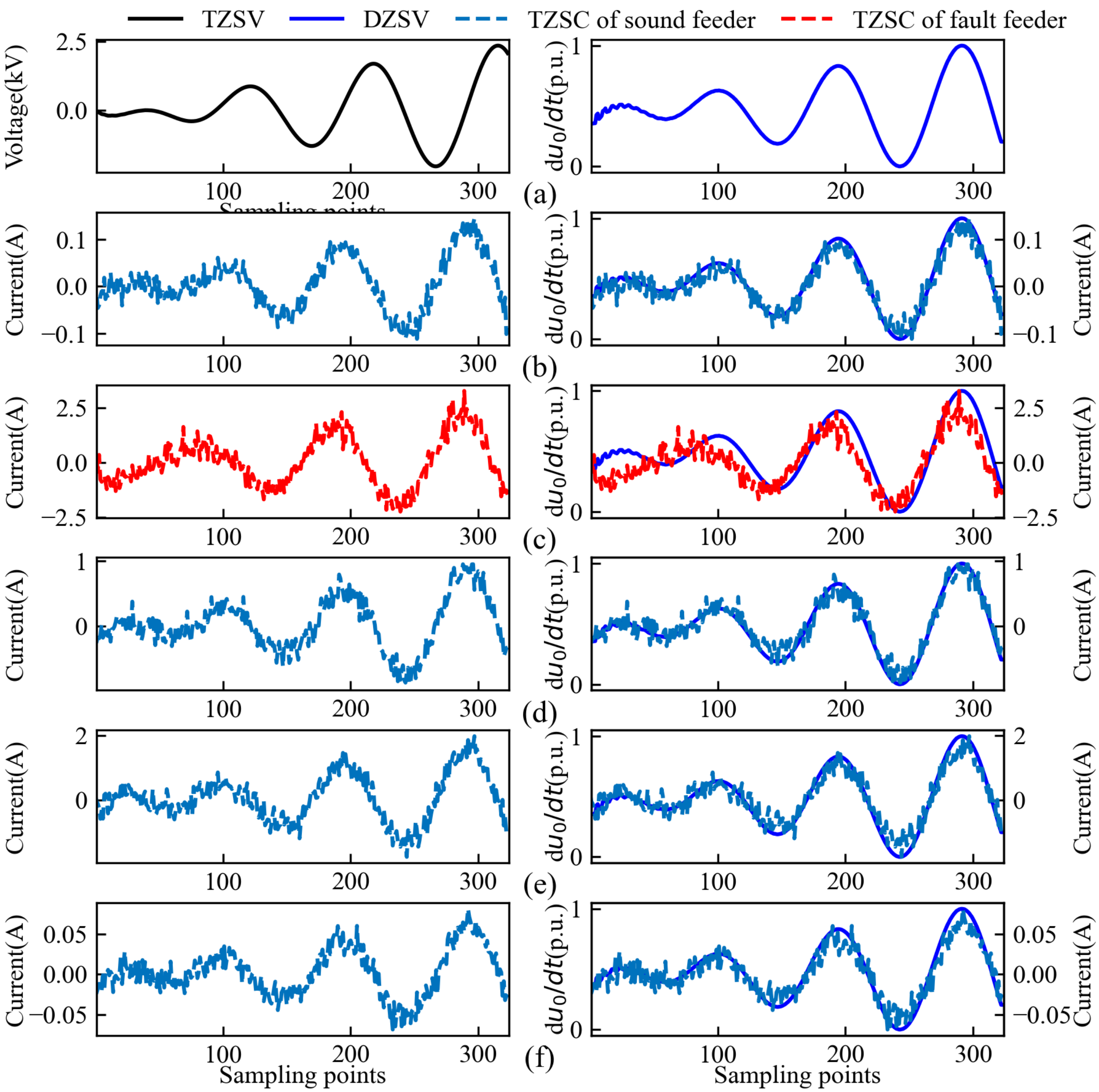

Fig. 12. Analysis of voltage and current waveforms under noise interference (l_2 fault, 3000Ω, SNR=20dB): (a) displays the voltage signals measured at the bus, while (b) through (f) depicts the current signals measured from the five feeders, corresponding to l_1, l_2, l_3, l_4, and l_5.

Table 7

CCD of diverse feeders under noise interference

SNR(dB)	l_1	l_2	l_3	l_4	l_5	Fault feeder
20	0.148	**-0.314**	0.204	0.134	0.184	l_2
25	0.302	**-0.339**	0.317	0.293	0.304	l_2
30	0.355	**-0.345**	0.386	0.342	0.450	l_2
35	0.361	**-0.345**	0.413	0.415	0.439	l_2

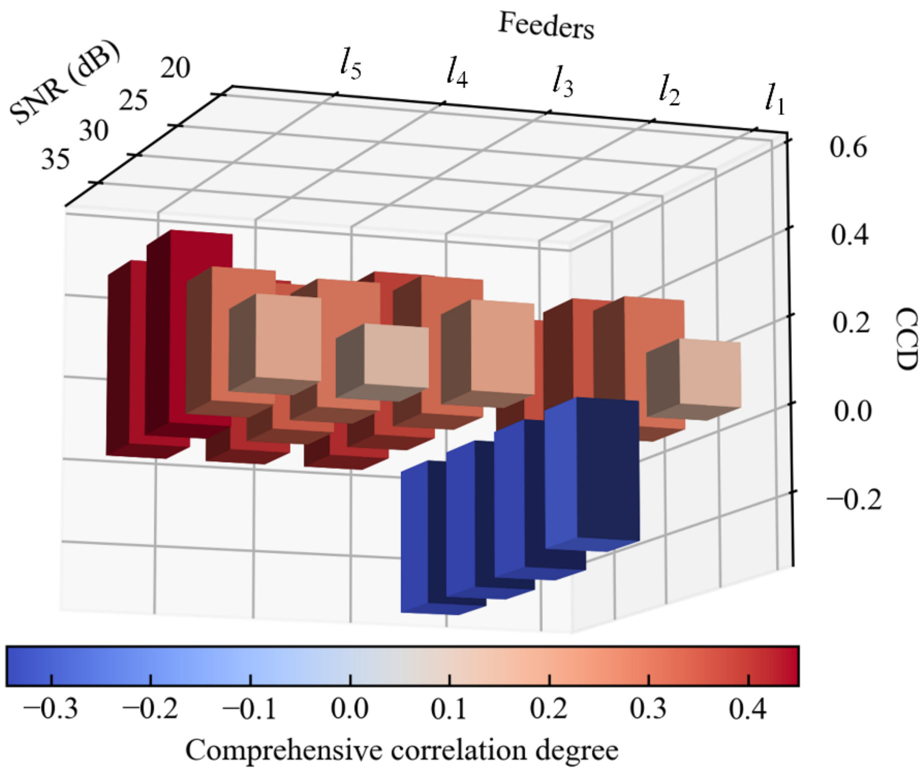

Fig. 13. CCD for each feeder under varied noise interference conditions

5.5.2 Topology Variation

Because the proposed approach enables fault feeder/section localization based solely on local ZSV and ZSC signals, it is immune to topology variations. Due to space limitations, verification results for the modified IEEE 13-node and 34-node distribution networks are provided.

Fig. 14 represents the modified IEEE 13-node distribution network, which is characterized by its short, high-load feeder, a single voltage regulator, diverse feeder types including both overhead and underground lines, shunt capacitors, and an in-line transformer, as referred to in [21]. The network is segmented into five feeders, which are indicated by the node combinations 632-646 (l_1), 632-634 (l_2), 671-611 (l_3), 671-675 (l_4), and 632-680 (l_5), each denoted with distinct colors for clarity.

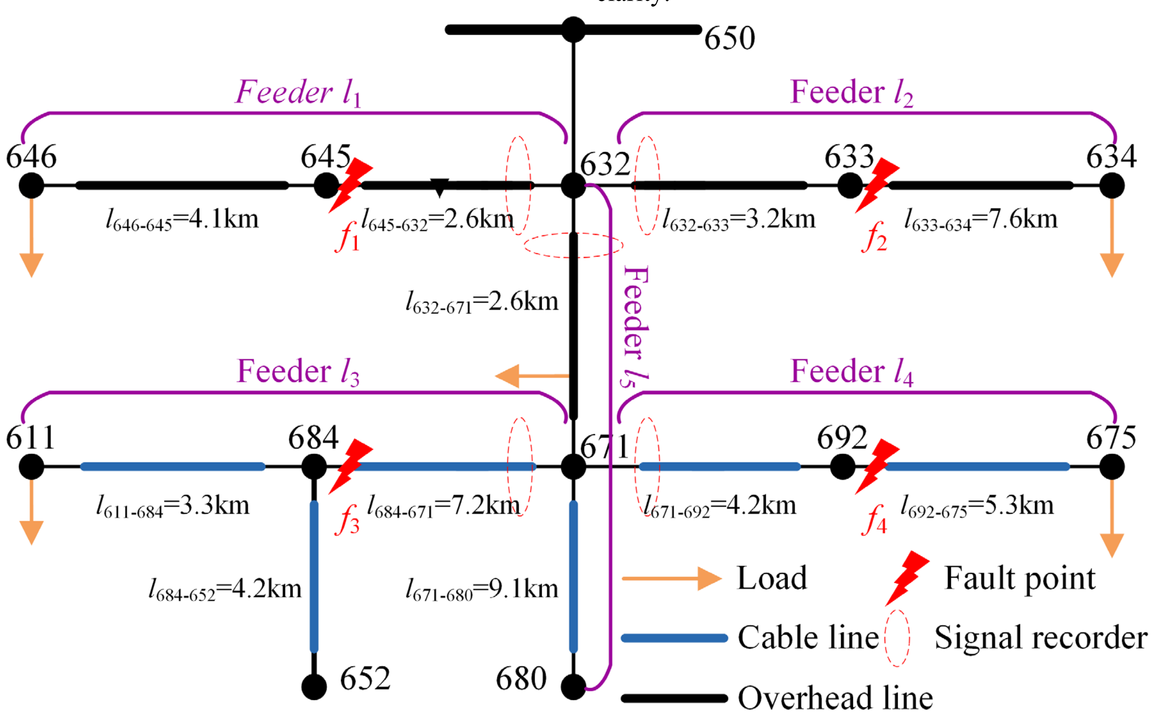

Fig. 14. IEEE-13 node distribution network.

The analysis incorporated a series of fault scenarios, exploring four FPs (f_1, f_2, f_3, f_4) represented by red lightning bolt symbols and two FRs (500 and 1000 Ω). A significant observation was noted when a HIF with a resistance of 1000 Ω was simulated at FP f_3 located at the end of feeder l_3. As depicted in Fig. 15, this fault resulted in a noticeable polarity variation between the DZSV and TZSC for the fault feeder l_3, contrasted with the operational state of the other feeders (l_1, l_2, l_4, and l_5).

The CCD values for each feeder under the described fault conditions are listed in Table 8, showcasing the effectiveness of the proposed approach in detecting the fault feeder. The negative CCD value of feeder l_1 (-0.534) under FP f_1 with an FR of 500 Ω identifies it as the fault feeder, as opposed to the positive CCD values recorded for the other feeders. This pattern of a pronounced negative CCD value is consistently observed in feeder l_2 under FP f_2, feeder l_3 under FP f_3 with an FR of 1000 Ω, and feeder l_4 under FP f_4, effectively distinguishing each as the fault feeder when compared to the positive CCD values of the sound feeders.

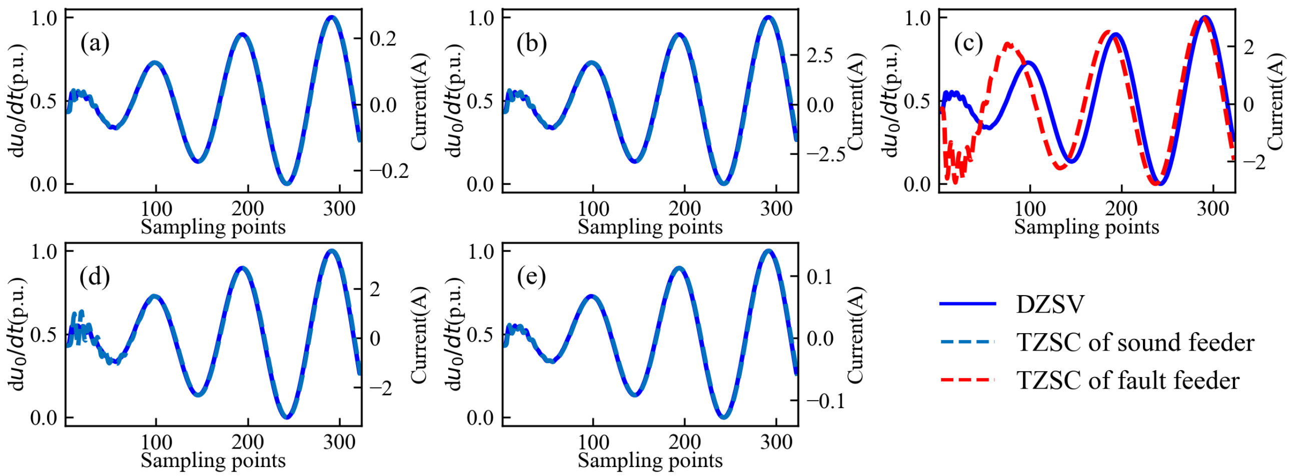

Fig. 15. DZSV and TZSC waveforms collected from diverse feeders (l_3 fault, 1000 Ω). (a) l_1 (b) l_2 (c) l_3 (d) l_4 (e) l_5.

Table 8

CCD of diverse feeders under IEEE-13 node distribution network

FP	FR	l_1	l_2	l_3	l_4	l_5	Fault feeder
f_1	500	**-0.534**	0.463	0.457	0.453	0.465	l_1
f_2		0.457	**-0.446**	0.453	0.370	0.463	l_2
f_3	1000	0.527	0.523	**-0.516**	0.485	0.528	l_3
f_4		0.533	0.528	0.299	**-0.499**	0.533	l_4

As shown in Fig. 16, the IEEE 34-node distribution network underscores that the fault localization task is specifically concentrated on pinpointing fault sections, not merely identifying faulted feeders [31], shifting the focus of our proposed approach from fault feeder detection to fault section location. This approach is directly applicable to locating fault sections without modifications. The detection result at each node identifies its position as either upstream or downstream of the fault point. The fault section can be accurately determined by aggregating these results and signal recorder information.

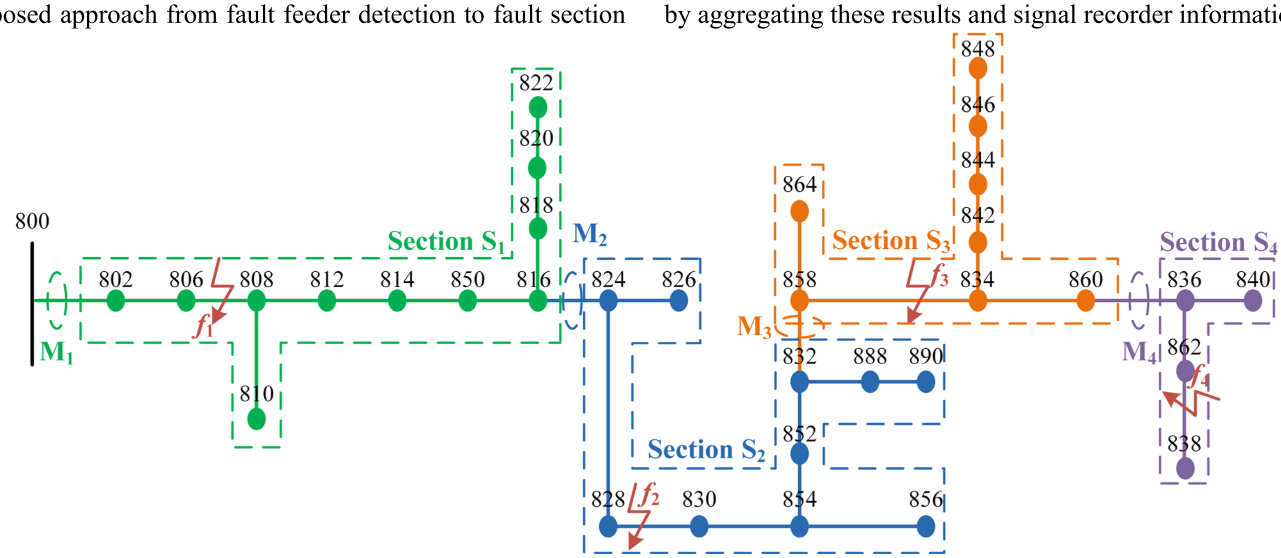

Fig. 16. IEEE-34 node distribution network.

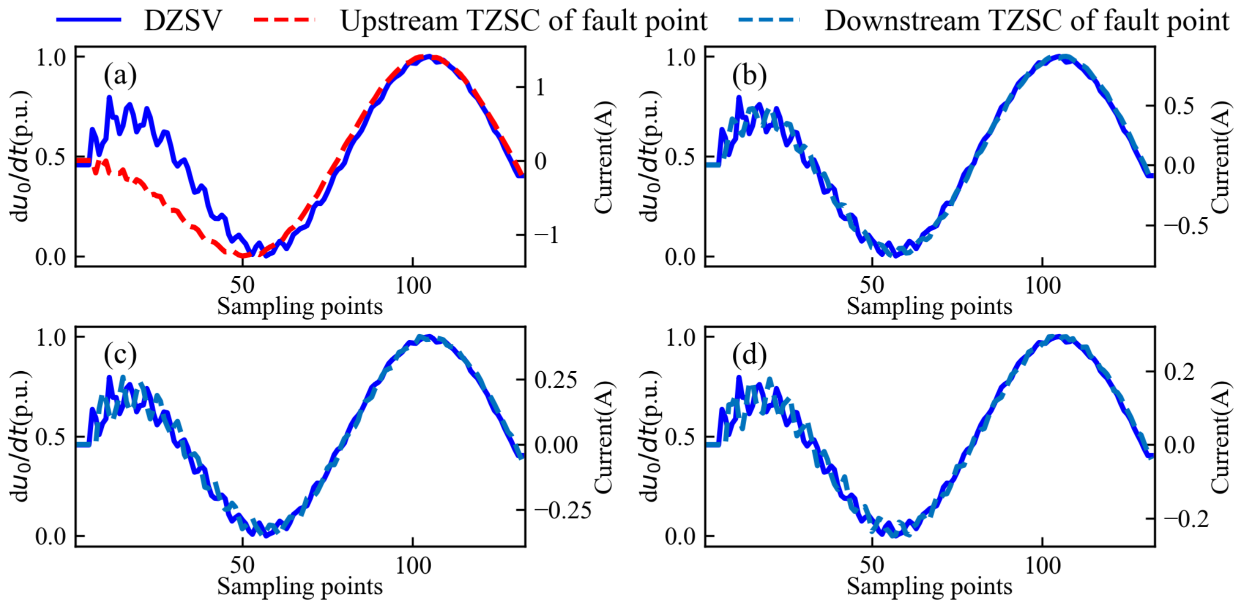

Fig. 17. DZSV and TZSC waveforms collected from diverse sections (S_1 fault, 1500Ω). (a) M_1 (b) M_2 (c) M_3 (d) M_4.

In Fig. 17, the DZSV and TZSCs waveforms from signal recorders M_1 to M_4 are depicted for a fault scenario involving a 1500 Ω resistance at f_1 in section S_1. The waveforms exhibit a significant discrepancy in the DZSV and the TZSC at the fault's upstream node, captured by recorder M_1, where a negative CCD of -0.45 is observed. Conversely, at downstream nodes, recorded by M_2, M_3, and M_4, consistent polarity and positive CCD values of 0.43, 0.35, and 0.35, respectively, are maintained. These distinct waveform characteristics and CCD values are pivotal for the proposed approach to identify fault section S_1 accurately.

Table 9 presents the CCD values of diverse signal recorders for different faults in the IEEE 34-node network, allowing for a thorough quantitative analysis. The table lists CCD values associated with each fault point and signal recorder, which collectively provide a decisive identification of the fault sections. For example, for a fault at f_2, the negative CCDs at M_1 and M_2, -0.50 and -0.44, determine these nodes as upstream, while the positive CCDs at M_3 and M_4 identify these as downstream, thereby localizing the fault to section S_2. This pattern of CCD values is consistently replicated for faults at f_3 and f_4, with the CCDs effectively delineating the fault sections S_3 and S_4. These quantitative details reinforce the proposed approach's validity and exhibit its capability for precise fault section localization within the IEEE 34-node distribution network.

Table 9

CCD of diverse signal recorders under IEEE-34 node distribution network

FP	FR	M_1	M_2	M_3	M_4	Fault section
f_1	1500	**-0.45**	0.43	0.35	0.35	S_1
f_2		**-0.50**	**-0.44**	0.37	0.36	S_2
f_3	2000	**-0.47**	**-0.42**	**-0.60**	0.19	S_3
f_4		**-0.47**	**-0.45**	**-0.59**	**-0.49**	S_4

6. Experimental verification

6.1 Engineering Deployment

A custom-built industrial prototype was created to examine the proposed approach for HIF localization in practical engineering applications. The prototype, intended for mounting on a 10 kV distribution feeder pole, seamlessly integrates with the existing primary-secondary fusion switch, as illustrated in Fig. 18. The distinctive aspect of this prototype compared to commercial counterparts lies in its unique hardware structure and software framework, all designed to fulfill real-time fault diagnosis requirements. The hardware structure, depicted in Fig. 18(c), divides the prototype into data acquisition and processing modules. The former consists of a microprocessor control unit (MCU) and an analog-to-digital converter (ADC) using STM32 and AD7606 chips, respectively. These components establish a serial peripheral interface (SPI) communication channel, with the MCU receiving signals from voltage and current transformers collected by the ADC. Subsequently, the data is transmitted to the data processing module—a RaspPi board equipped with the proposed approach.

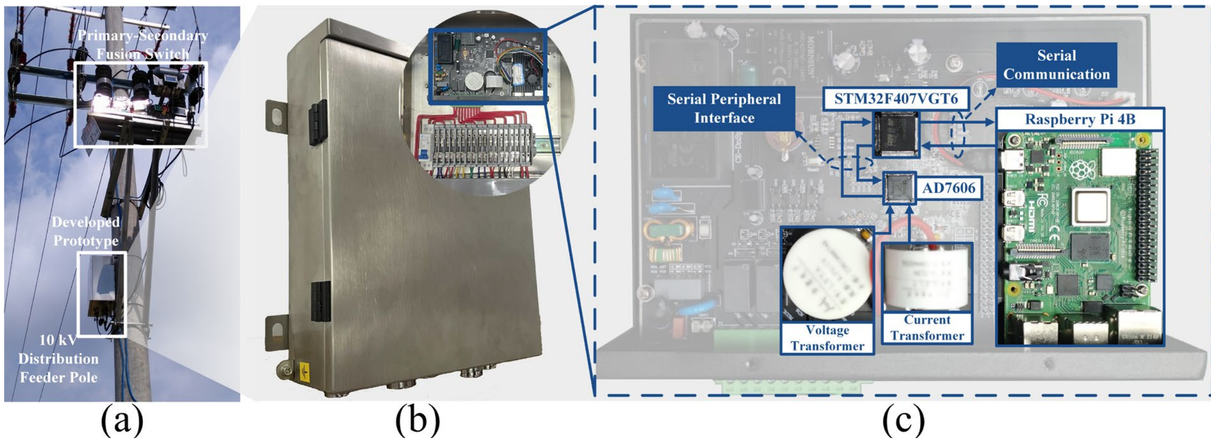

Fig. 18. Engineering deployment of the industrial prototype.
(a) Application scenarios (b) Device main unit (c) Hardware structure.

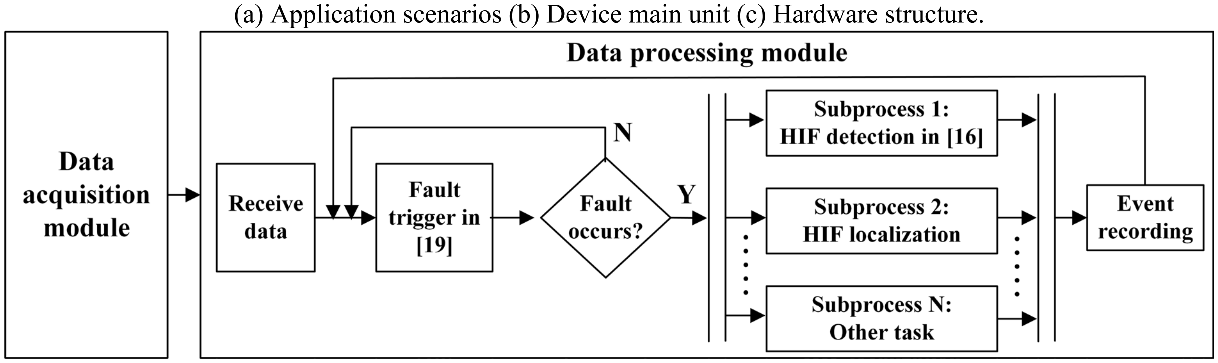

Fig. 19. Software framework of the industrial prototype.

Table 10
Computation complexity of the proposed approach.

Computation metric	Adaptive TP calibration	Multiscale correlation analysis
Model	1D-Unet	N/A
FLOPs	1.35 G	
Model size	18.25 MB	
Trainable parameter size	1.58 M	
Training device	NVIDIA® GeForce RTX-1060 GPU	
Training time	16 min	
Edge device	Raspberry Pi 4B	Raspberry Pi 4B
Individual inference time	15.78 ms	56.67 ms
Total inference time	71.45 ms	

Incorporating a multi-process technique, the software framework in Fig. 19 enables multitasking parallel processing with the potential for further expansion. Tasks like HIF detection and fault localization are independently performed without interference. Upon receiving data from the data acquisition module, the main process in the data processing module employs the fault trigger approach from [19] to identify potential faults. Multiple subprocesses are then initiated to execute diverse tasks simultaneously, such as fault localization or HIF detection.

The computational complexity of the proposed method is detailed in Table 10. The adaptive TP calibration utilizes a 1D-Unet model, requiring 1.35 billion floating point operations per second (FLOPs), which highlights the substantial computational demands of the model. Despite these demands, the 1D-Unet model's size is only 18.25 MB, with 1.58 million trainable parameters, ensuring that the model is sufficiently compact for training on conventional GPUs. The training was conducted effectively on an NVIDIA® GeForce RTX-1060 GPU and completed within 16 minutes. For deployment in a real-world setting, the Raspberry Pi 4B served as the edge device in both the calibration and analysis phases, affirming the model's suitability for widely-used, low-power computing environments. The inference times are notably practical, with the adaptive TP calibration and the multiscale correlation analysis requiring just 15.78 milliseconds and 56.67 milliseconds, respectively. Consequently, the total inference time for the proposed approach stands at 71.45 milliseconds, well within the parameters necessary for real-time task execution.

6.2 Experimental Test

Fig. 20 depicts the laboratory testing scenario for our industrial prototype, detailing the intricate setup where a personal computer controls a relay protection tester via an Ethernet cable. This setup reproduces field fault waveforms, allowing for a high-fidelity simulation of real-world scenarios. The tester interfaces with the prototype for data acquisition, while a digital oscilloscope displays the waveforms in real time, facilitating immediate visual analysis. Results presentation and distributed debugging functions are streamlined through a user-friendly interface, enhancing the efficiency of the prototype's operation.

As visualized in Fig. 21, the test system comprises a full-scale 10 kV network with four feeders and a specialized fault simulation module. This module adeptly simulates HIFs using a rotating mechanical arm that contacts various high-impedance materials, demonstrating the system's versatility in replicating different fault conditions.

Fig. 22 presents the waveform recordings from this system during HIF incidents involving diverse materials such as branches, grass, gravel, and arcs within the cable. The waveforms for the DZSC and TZSC display a pronounced polarity inversion in the fault feeder compared to the consistent polarity in sound feeders for each material tested.

These waveform characteristics are quantitatively corroborated by Table 11, which lists the CCD values for each fault scenario. The table identifies feeder l_1 as the fault feeder with negative CCD values: -0.49 for branches, -0.61 for grass, -0.56 for gravel, and -0.56 for an arc, distinctly contrasted with the positive CCD values of the sound feeders l_2, l_3, and l_4. These quantitative results, consistent with the visual evidence from Fig. 22, validate the efficacy of our prototype across diverse HIF scenarios, demonstrating its capability to localize fault feeder within a complex practical distribution network accurately.

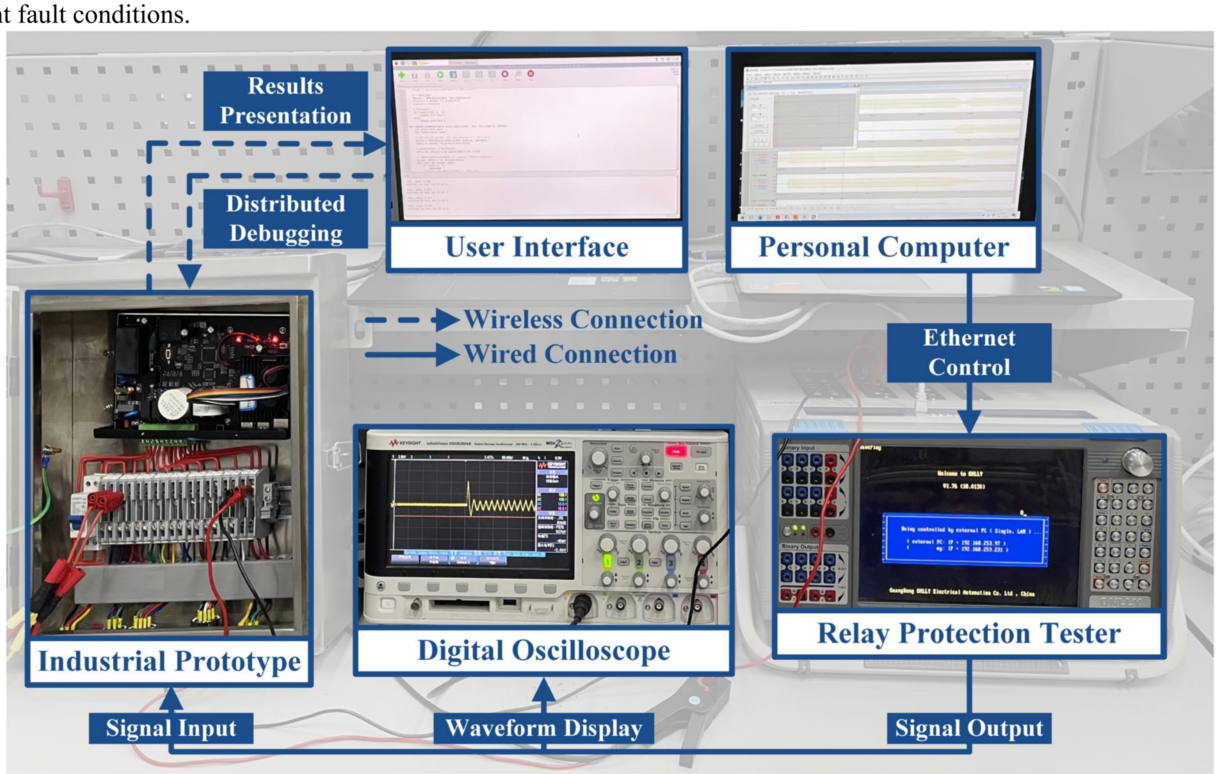

Fig. 20. Laboratory testing scenario of industrial prototype.

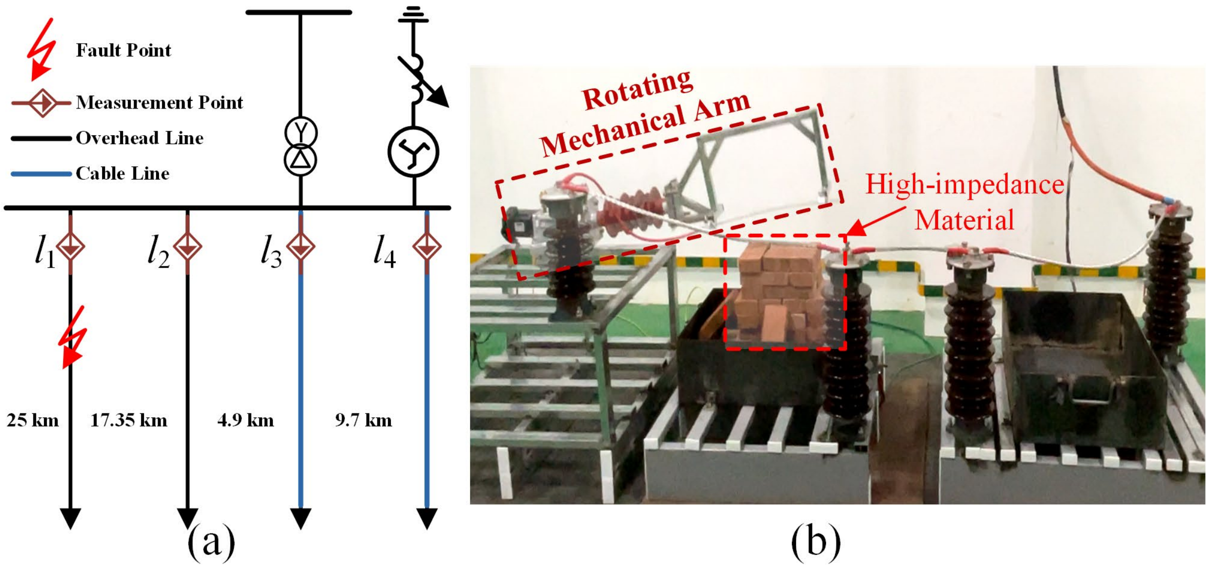

Fig. 21. 10kV full-scale test system. (a) System topology. (b) Fault simulation module.

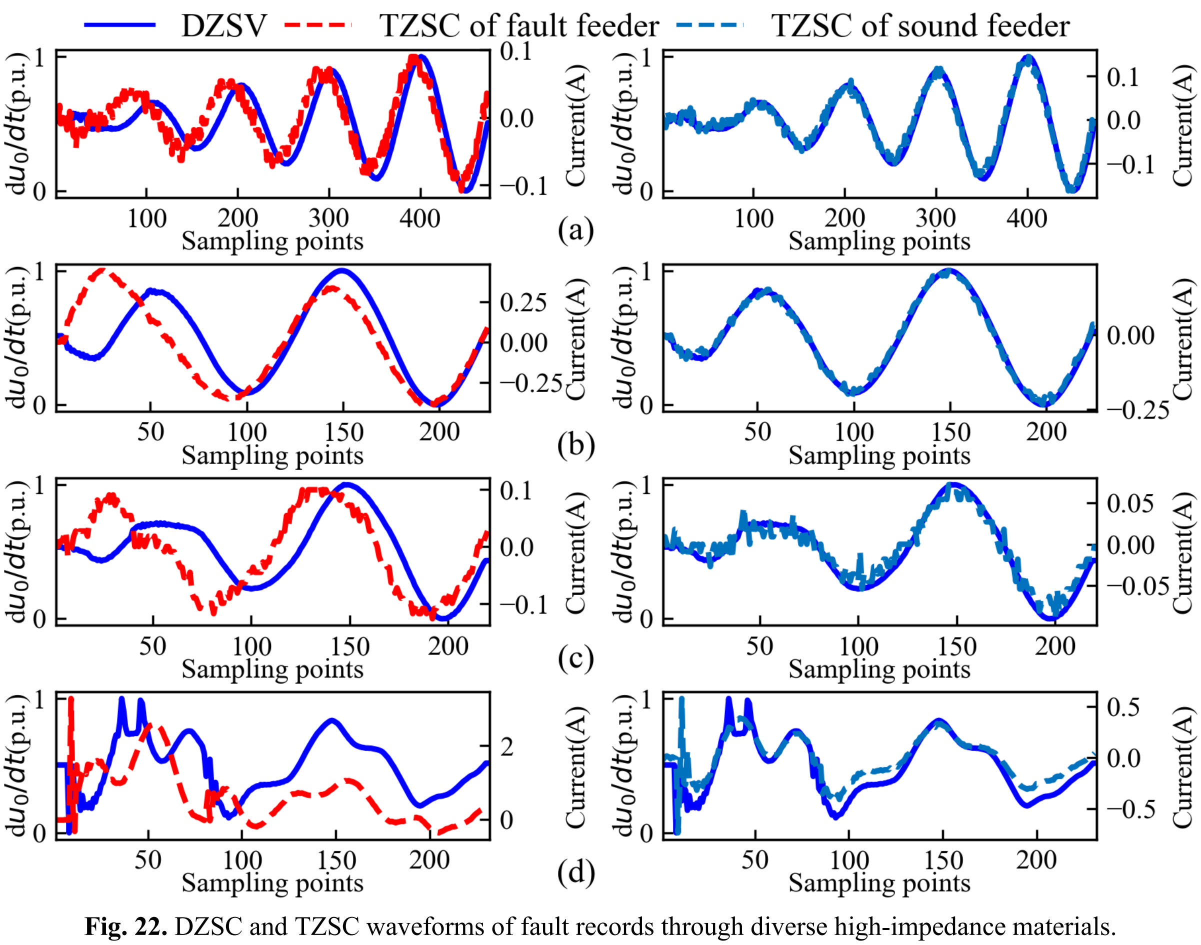

Fig. 22. DZSC and TZSC waveforms of fault records through diverse high-impedance materials.
(a) Branches. (b) Grass. (c) Gravel. (d) Arc in the cable.

Table 11
CCD under 10kV full-scale test system

Fault scenario	l_1	l_2	l_3	l_4	Fault feeder
Branches	**-0.49**	0.43	0.31	0.11	l_1
Grass	**-0.61**	0.90	0.97	0.50	l_1
Gravel	**-0.56**	0.57	0.79	0.27	l_1
Arc in the cable	**-0.56**	0.71	0.74	0.63	l_1

6.3 Comparative Analysis

A comparative analysis was executed on a 10kV full-scale test system, juxtaposing the proposed approach with the typical methods cited in [31], [35], [36]. Method [31] targets the extremities of various ZSCs, including their maxima and minima, to calculate the comprehensive inner product values (CIPV) for fault feeder identification. This technique proves efficient when fault and sound feeders' polarity remains unchanged post-SPGF. Nonetheless, the Peterson coil's influence causes an alignment of polarities once stability is achieved, as evidenced in Fig. 22.

Table 12

Comparison results with typical methods

(a) The judgment results of the method in [31]

Fault feeder	Fault conditions	No.	l_1	l_2	l_3	l_4	Result
l_1	Grass	1	-0.033	-0.018	**-0.036**	-0.011	Error
		2	**-0.033**	0.035	-0.024	0.012	
		3	**-0.031**	0.054	-0.012	0.017	
		4	**-0.037**	0.065	-0.018	0.021	
		5	**-0.033**	0.069	-0.009	0.022	
		6	**-0.037**	0.068	-0.016	0.026	

(b) The judgment results of the method in [35]

Fault feeder	Fault conditions	TS_k				TS_{set}	Result
		TS_1	TS_2	TS_3	TS_4		
l_1	Grass	**12.324**	0.476	1.774	0.264	3.213	l_1
l_2	200Ω	**69.193**	**76.591**	58.003	5.228	58.145	l_1, l_2
l_3	2000Ω	10.043	2.0031	**32.672**	1.066	11.950	l_3
l_4	2000Ω	**13.973**	2.620	**11.263**	**12.187**	11.020	l_1, l_2, l_4

(c) The judgment results of the method in [36]

Fault feeder	Fault conditions	Calculated [ρ_1, ρ_2, ρ_3, ρ_4]	Calculated [E_1, E_2, E_3, E_4] $*10^{-3}$	Result
l_1	Grass	[0.212, 0.725, 0.735, 0.712]	[**59.96,** 0.81, 6.69, 0.26]	l_1
l_2	200Ω	[0.714, **-0.327,** 0.753, 0.650]	/	l_2
l_3	2000Ω	[0.683, 0.689, 0.516, 0.775]	[7.85, 4.93, **21.24,** 0.78]	l_3
l_4	2000Ω	[0.161, 0.137, **-0.885,** -**0.942**]	[2.43, 1.17, **102.58,** 2.83]	l_3

(d) The judgment results of the proposed approach

Fault feeder	Fault conditions	CCD	Result
l_1	Grass	[**-0.609,** 0.901, 0.974, 0.570]	l_1
l_2	200Ω	[0.949, **-0.677,** 0.977, 0.589]	l_2
l_3	2000Ω	[0.651, 0.671, **-0.289,** 0.078]	l_3
l_4	2000Ω	[0.776, 0.376, 0.890, **-0.578**]	l_4

As per [31], a negative CIPV suggests a feeder fault, with the smallest value indicating the faulted feeder. Yet, Table 12(a) highlights the method's shortcomings, particularly when HIF occurs in grass. Initially, the CIPVs at the first extreme point are all negative values. Among them, the maximum CIPV indicates feeder l_3 as the fault feeder. However, at the following four extreme points, there existed two negative and two positive values for each extreme point, whose confusing results present a dichotomy that undermines fault feeder detection.

Method [35] introduces a synthesis of transient and steady-state factors derived from both the transient stage and the steady-state component of the fault's zero-sequence equivalent network. Table 12(b) demonstrates the limitations of this method during HIF grounded with grass, where TS_1 (12.324) significantly surpasses TS_2 (0.476), TS_3 (1.774), TS_4 (0.264) and TS_{set} (3.213), accurately identifying feeder l_1 as the fault feeder. However, the method occasionally results in multiple false indications. Specifically, for the SPGF through low resistance of 200 Ω on feeder l_2, the corresponding TS_1 (69.193) and TS_2 (76.591) far exceed TS_3 (58.003), TS_4 (5.228) and TS_{set} (58.145), leading to the incorrect identification of feeders l_1 and l_2 as faulted due to their elevated TS values relative to TS_{set}. Likewise, for a SPGF through a high resistance of 2000 Ω on feeder l_4, TS_1 (13.973), TS_3 (11.263), and TS_4 (12.187) substantially outstrip TS_2 (2.620) and TS_{set} (11.020), erroneously identifying feeders l_1, l_3, and l_4 as fault feeder. Such inaccuracies could increase maintenance efforts and limit the method's practical utility.

Method [36] combines the correlation between ZSC and ZSV with harmonic energy, similar to our approach that leverages transient information for detecting the fault feeder. While this method generally outperforms others across a range of fault conditions, including HIF and SPGF at low resistance levels, it could not identify the fault feeder under a 2000 Ω SPGF condition on feeder l_4, as evidenced in Table 12(c). The analysis, using waveform correlation and harmonic energy, revealed through two arrays [0.161, 0.137, **-0.885, -0.942**] and [2.43, 1.17, **102.58,** 2.83], suggests feeders l_3 and l_4 as potential fault sources. However, the harmonic energy indicator incorrectly the sound feeder l_3 as the fault.

Our approach demonstrates exceptional localization accuracy and versatility across various fault conditions, including HIF and SPGF, at both low and high resistances. As shown in Table 12(d), our approach flawlessly identifies the correct fault feeder under every tested condition, evidenced by distinct negative CCD values for fault conditions, such as -0.609 for a fault in the grass at feeder l_1. Conversely, sound feeders exhibit positive CCD values, exemplified by 0.901 for feeder l_2, 0.974 for l_3, and 0.570 for l_4, showcasing our approach's precise fault localization capabilities in complex distribution networks. The detailed results further corroborate the accuracy of our approach, with CCD values clearly distinguishing the fault feeder in various scenarios: feeder l_1 under HIF grounded with grass, feeder l_2 with a 200Ω fault, feeder l_3 with a 2000Ω fault, and feeder l_4 also with a 2000Ω fault, demonstrating the approach's robustness and reliability.

7. Discussion

The paper adopted a split-and-conquer strategy for HIF localization, including adaptive TP calibration and multiscale correlation analysis. This innovative approach leverages AI techniques and domain knowledge to improve fault localization accuracy. The adaptive calibration stage, essential to our approach, resembles pixel classification in image semantic segmentation, for which the Unet architecture is specifically designed. The Unet model's encoder-decoder structure enables it to capture local and global features, enhancing classification performance even in 1D sequential data analysis, which inspired us to use the 1D-UNet model as the core network structure, aiding multiscale correlation analysis in fault localization tasks by focusing on transient information from SPGF or HIF.

However, the 1D-Unet model's efficiency may be compromised by noise in the data, including environmental and quantization noise. The latter, resulting from analog-to-digital conversion, can obscure the TZSC in digital signals, leading to potential misjudgments. It's been found that the model performs effectively within an environmental noise threshold of 20 dB, but quantization noise remains a challenge, particularly when it causes indistinct TZSCs. Addressing these vague signals is crucial for improving fault localization methods.

Furthermore, the effectiveness of the proposed approach is contingent upon the fault-triggering technique. While our approach generally tolerates minor deviations from these methods, it relies on the presence of accurate fault moments. The absence of this moment hampers the ability to perform adaptive TP calibration and multiscale correlation analysis, resulting in the potential failure of the approach under such circumstances.

8. Conclusion

This paper introduces an advanced HIF localization approach through adaptive TP calibration and multiscale correlation analysis to enhance HIF localization in active distribution networks. This approach incorporates the semantic segmentation model, namely 1D-Unet, to facilitate sample point classification and distinguish whether the sample points are part of the TP associated with SPGF. Given HIF's longer transient duration than LIF, the adaptive TP calibration effectively extracts comprehensive transient information for subsequent multiscale correlation analysis. In conjunction with the Pearson correlation coefficient, a sliding window strategy calculates the LCD between DZSV and TZSC, enabling micro-scale correlation of transient information. Consequently, the CCD is a macro-scale criterion for localizing the fault feeder or section.

The validation of this approach includes both simulation and experimental verification. Initially, the 1D-Unet model is trained with simulation data from the PSCAD/EMTDC platform, demonstrating high accuracy in sample point classification with a success rate of 99.2% in test sets. Further analysis of the method's adaptability reveals its robustness against noise interference up to 20 dB and its effectiveness in networks with varying topologies, such as the IEEE-13 and 34-node distribution networks, through multiscale correlation analysis.

An industrial prototype was developed to apply this method in real-world scenarios, tested within a 10 kV full-scale test system. The comparative analysis underscores its superiority over the typical methods in localizing HIFs, including faults grounded with grass, SPGF with 200 Ω, and 2000 Ω across different fault feeders. Unlike the misjudgments commonly associated with the typical methods, our approach demonstrates effective performance under various fault conditions.

Nevertheless, this approach is not without its limitations. Firstly, quantization noise in data acquisition may obscure waveforms and hinder the correlation between DZSV and TZSC, potentially leading to incorrect judgments. Secondly, while minor discrepancies in fault-triggering methods do not affect the performance, an inability to detect the precise moment of fault occurrence complicates the TP calibration with the 1D-Unet.

9. Future work

Future work will focus on enhancing the practicality of the proposed approach by integrating it with conventional fault localization methods that utilize transient information. Furthermore, the impact of quantization noise on the AI model's ability to classify faults accurately will be thoroughly investigated. This investigation will include developing strategies to mitigate the effects of quantization noise or adaptively incorporate them into the model's decision-making process. Moreover, the research will address the challenges associated with the misjudgment of fault-triggering methods for HIF to improve the accuracy and reliability of these methods.

The future direction seeks to refine the proposed approach for fault localization in active distribution networks, ensuring it remains effective and reliable across a broad spectrum of fault scenarios.

CRediT authorship contribution statement

Jian-Hong Gao: Conceptualization, Methodology, Writing-Original draft preparation. **Mou-Fa Guo:** Supervision, Validation. **Shuyue Lin**: Reviewing and Editing. **Duan-Yu Chen**: Software, Data curation

Declaration of competing interest

The authors declare that they have no known competing financial interests or personal relationships that could have appeared to influence the work reported in this paper.

Acknowledgments

This work was supported in part by the National Natural Science Foundation of China through the Project of Research of Flexible and Adaptive Arc-Suppression Method for Single-Phase Grounding Fault in Distribution Networks under Project 51677030.

References

[1] M. Mishra and R. R. Panigrahi, 'Taxonomy of high impedance fault detection algorithm', *Measurement*, vol. 148, p. 106955, Dec. 2019, doi: 10.1016/j.measurement.2019.106955.

[2] X. Song, P. Sun, S. Song, and V. Stojanovic, 'Finite-time adaptive neural resilient DSC for fractional-order nonlinear large-scale systems against sensor-actuator faults', *Nonlinear Dyn.*, vol. 111, no. 13, pp. 12181–12196, Jul. 2023, doi: 10.1007/s11071-023-08456-0.

[3] X. Song, N. Wu, S. Song, Y. Zhang, and V. Stojanovic, 'Bipartite synchronization for cooperative-competitive neural networks with reaction–diffusion terms via dual event-triggered mechanism', *Neurocomputing*, vol. 550, p. 126498, Sep. 2023, doi: 10.1016/j.neucom.2023.126498.

[4] X. Song, N. Wu, S. Song, and V. Stojanovic, 'Switching-Like Event-Triggered State Estimation for Reaction–Diffusion Neural Networks Against DoS Attacks', *Neural Process. Lett.*, vol. 55, no. 7, pp. 8997–9018, Dec. 2023, doi: 10.1007/s11063-023-11189-1.

[5] Z. Zhang, X. Song, X. Sun, and V. Stojanovic, 'Hybrid-driven-based fuzzy secure filtering for nonlinear parabolic partial differential equation systems with cyber attacks', *Int. J. Adapt. Control Signal Process.*, vol. 37, no. 2, pp. 380–398, Feb. 2023, doi: 10.1002/acs.3529.

[6] M. Zafeiropoulou *et al.*, 'A Flexibility Platform for Managing Outages and Ensuring the Power System's Resilience during Extreme Weather Conditions', *Processes*, vol. 11, no. 12, p. 3432, Dec. 2023, doi: 10.3390/pr11123432.

[7] G. Fotis, V. Vita, and T. I. Maris, 'Risks in the European Transmission System and a Novel Restoration Strategy for a Power System after a Major Blackout', *Appl. Sci.*, vol. 13, no. 1, p. 83, Dec. 2022, doi: 10.3390/app13010083.

[8] J. Fang, K. Chen, C. Liu, and J. He, 'An Explainable and Robust Method for Fault Classification and Location on Transmission Lines', *IEEE Trans. Ind. Inform.*, vol. 19, no. 10, pp. 10182–10191, Oct. 2023, doi: 10.1109/TII.2022.3229497.

[9] T. Biswal and S. K. Parida, 'A novel high impedance fault detection in the micro-grid system by the summation of accumulated difference of residual voltage method and fault event classification using discrete wavelet transforms and a decision tree approach', *Electr. Power Syst. Res.*, vol. 209, p. 108042, Aug. 2022, doi: 10.1016/j.epsr.2022.108042.

[10] G. N. Lopes, T. S. Menezes, G. G. Santos, L. H. P. C. Trondoli, and J. C. M. Vieira, 'High Impedance Fault detection based on harmonic energy variation via S-transform', *Int. J. Electr. Power Energy Syst.*, vol. 136, p. 107681, Mar. 2022, doi: 10.1016/j.ijepes.2021.107681.

[11] F. Hojatpanah, F. Badrkhani Ajaei, and H. Tiwari, 'Reliable detection of high-impedance faults using mathematical morphology', *Electr. Power Syst. Res.*, vol. 216, p. 109078, Mar. 2023, doi: 10.1016/j.epsr.2022.109078.

[12] K. S. V. Swarna, A. Vinayagam, M. Belsam Jeba Ananth, P. Venkatesh Kumar, V. Veerasamy, and P. Radhakrishnan, 'A KNN based random subspace ensemble classifier for detection and discrimination of high impedance fault in PV integrated power network', *Measurement*, vol. 187, p. 110333, Jan. 2022, doi: 10.1016/j.measurement.2021.110333.

[13] R. Soni and B. Mehta, 'Diagnosis and prognosis of incipient faults and insulation status for asset management of power transformer using fuzzy logic controller & fuzzy clustering means', *Electr. Power Syst. Res.*, vol. 220, p. 109256, Jul. 2023, doi: 10.1016/j.epsr.2023.109256.

[14] A. Srivastava and S. K. Parida, 'A Robust Fault Detection and Location Prediction Module Using Support Vector Machine and Gaussian Process Regression for AC Microgrid', *IEEE Trans. Ind. Appl.*, vol. 58, no. 1, pp. 930–939, Jan. 2022, doi: 10.1109/TIA.2021.3129982.

[15] M.-F. Guo, X.-D. Zeng, D.-Y. Chen, and N.-C. Yang, 'Deep-Learning-Based Earth Fault Detection Using Continuous Wavelet Transform and Convolutional Neural Network in Resonant Grounding Distribution Systems', *IEEE Sens. J.*, vol. 18, no. 3, pp. 1291–1300, Feb. 2018, doi: 10.1109/JSEN.2017.2776238.

[16] Q.-M. Xiao, M.-F. Guo, and D.-Y. Chen, 'High-Impedance Fault Detection Method Based on One-Dimensional Variational Prototyping-Encoder for Distribution Networks', *IEEE Syst. J.*, vol. 16, no. 1, pp. 966–976, Mar. 2022, doi: 10.1109/JSYST.2021.3053769.

[17] C. Hong, H.-Y. Qiu, J.-H. Gao, S. Lin, and M.-F. Guo, 'Semantic Segmentation-Based Intelligent Threshold-Free Feeder Detection Method for Single-Phase Ground Fault in Distribution Networks', *IEEE Trans. Instrum. Meas.*, vol. 73, pp. 1–9, 2024, doi: 10.1109/TIM.2023.3335520.

[18] Z. Chen, M. Wang, M. Zhang, W. Huang, H. Gu, and J. Xu, 'Post-processing refined ECG delineation based on 1D-UNet', *Biomed. Signal Process. Control*, vol. 79, p. 104106, Jan. 2023, doi: 10.1016/j.bspc.2022.104106.

[19] J.-H. Gao, M.-F. Guo, S. Lin, and D.-Y. Chen, 'Application of semantic segmentation in High-Impedance fault diagnosis combined signal envelope and Hilbert marginal spectrum for resonant distribution networks', *Expert Syst. Appl.*, vol. 231, p. 120631, Nov. 2023, doi: 10.1016/j.eswa.2023.120631.

[20] Y. Wang *et al.*, 'Faulty Feeder Detection of Single Phase-Earth Fault Using Grey Relation Degree in Resonant Grounding System', *IEEE Trans. Power Deliv.*, vol. 32, no. 1, pp. 55–61, Feb. 2017, doi: 10.1109/TPWRD.2016.2601075.

[21] X. Wang, J. Gao, M. Chen, X. Wei, Y. Wei, and Z. Zeng, 'Faulty Line Detection Method Based on Optimized Bistable System for Distribution Network', *IEEE Trans. Ind. Inform.*, vol. 14, no. 4, pp. 1370–1381, Apr. 2018, doi: 10.1109/TII.2017.2753227.

[22] X. Wei, X. Wang, J. Gao, D. Yang, K. Wei, and L. Guo, 'Faulty Feeder Detection for Single-Phase-to-Ground Fault in Distribution Networks Based on Transient Energy and Cosine Similarity', *IEEE Trans. Power Deliv.*, vol. 37, no. 5, pp. 3968–3979, Oct. 2022, doi: 10.1109/TPWRD.2022.3142186.

[23] B. Wang and X. Cui, 'Nonlinear Modeling Analysis and Arc High-Impedance Faults Detection in Active Distribution Networks With Neutral Grounding via Petersen Coil', *IEEE Trans. Smart Grid*, vol. 13, no. 3, pp. 1888–1898, May 2022, doi: 10.1109/TSG.2022.3147044.

[24] Z. Jianwen, H. Hui, G. Yu, H. Yongping, G. Shuping, and L. Jianan, 'Single-phase ground fault location method for distribution network based on traveling wave time-frequency characteristics', *Electr. Power Syst. Res.*, vol. 186, p. 106401, Sep. 2020, doi: 10.1016/j.epsr.2020.106401.

[25] X. Wang *et al.*, 'Fault feeder detection method utilized steady state and transient components based on FFT backstepping in distribution networks', *Int. J. Electr. Power Energy Syst.*, vol. 114, p. 105391, Jan. 2020, doi: 10.1016/j.ijepes.2019.105391.

[26] T. Jin, F. Zhuo, and M. A. Mohamed, 'A Novel Approach Based on CEEMDAN to Select the Faulty Feeder in Neutral Resonant Grounded Distribution Systems', *IEEE Trans. Instrum. Meas.*, vol. 69, no. 7, pp. 4712–4721, Jul. 2020, doi: 10.1109/TIM.2019.2954009.

[27] X. Wang *et al.*, 'High Impedance Fault Detection Method Based on Variational Mode Decomposition and Teager–Kaiser Energy Operators

for Distribution Network', *IEEE Trans. Smart Grid*, vol. 10, no. 6, pp. 6041–6054, Nov. 2019, doi: 10.1109/TSG.2019.2895634.

[28] J. Gao, X. Wang, X. Wang, A. Yang, H. Yuan, and X. Wei, 'A High-Impedance Fault Detection Method for Distribution Systems Based on Empirical Wavelet Transform and Differential Faulty Energy', *IEEE Trans. Smart Grid*, vol. 13, no. 2, pp. 900–912, Mar. 2022, doi: 10.1109/TSG.2021.3129315.

[29] M.-F. Guo, J.-H. Gao, X. Shao, and D.-Y. Chen, 'Location of Single-Line-to-Ground Fault Using 1-D Convolutional Neural Network and Waveform Concatenation in Resonant Grounding Distribution Systems', *IEEE Trans. Instrum. Meas.*, vol. 70, pp. 1–9, 2021, doi: 10.1109/TIM.2020.3014006.

[30] J. Yuan and Z. Jiao, 'Faulty Feeder Detection for Single Phase-to-Ground Faults in Distribution Networks Based on Waveform Encoding and Waveform Segmentation', *IEEE Trans. Smart Grid*, pp. 1–1, 2023, doi: 10.1109/TSG.2023.3243026.

[31] X. Wang, J. Gao, X. Wei, L. Guo, G. Song, and P. Wang, 'Faulty Feeder Detection Under High Impedance Faults for Resonant Grounding Distribution Systems', *IEEE Trans. Smart Grid*, vol. 14, no. 3, pp. 1880–1895, May 2023, doi: 10.1109/TSG.2022.3216731.

[32] A. Peimankar and S. Puthusserypady, 'DENS-ECG: A deep learning approach for ECG signal delineation', *Expert Syst. Appl.*, vol. 165, p. 113911, Mar. 2021, doi: 10.1016/j.eswa.2020.113911.

[33] 'IEEE Recommended Practice and Requirements for Harmonic Control in Electric Power Systems', *IEEE Std 519-2014 Revis. IEEE Std 519-1992*, pp. 1–29, Jun. 2014, doi: 10.1109/IEEESTD.2014.6826459.

[34] J.-H. Gao, 'LabelSIG: Electrical Signal Labeler to Extract Information from Common Format for Transient Data Exchange Records'. Accessed: Jul. 26, 2023. [Online]. Available: https://github.com/Jianhong-Gao/LabelSIG

[35] T. Tang, X. Zeng, C. Huang, and Z. Li, 'Faulty feeder detection based on the composite factors in resonant grounding distribution system', *Electr. Power Syst. Res.*, vol. 189, p. 106578, Dec. 2020, doi: 10.1016/j.epsr.2020.106578.

[36] J. Yuan, Y. Hu, Y. Liang, and Z. Jiao, 'Faulty Feeder Detection for Single Line-to-Ground Fault in Distribution Networks With DGs Based on Correlation Analysis and Harmonics Energy', *IEEE Trans. Power Deliv.*, vol. 38, no. 2, pp. 1020–1029, Apr. 2023, doi: 10.1109/TPWRD.2022.3203992.